

**TRANSMISSION DOSIMETRY WITH A SCANNING LIQUID
FILLED ELECTRONIC PORTAL IMAGING DEVICE FOR
MEGAVOLTAGE PHOTON BEAMS**

by

HOMAYOON PARSAEI

B.Sc., Honors physics, University of Concordia

A THESIS SUBMITTED IN PARTIAL FULFILLMENT
OF THE REQUIREMENTS FOR THE DEGREE OF
MASTER OF SCIENCE

in

THE FACULTY OF GRADUATE STUDIES

Department of Physics

We accept this thesis as conforming
to the required standard

THE UNIVERSITY OF BRITISH COLUMBIA

March 1997

© Homayoon Parsaei, 1997

In presenting this thesis in partial fulfilment of the requirements for an advanced degree at the University of British Columbia, I agree that the Library shall make it freely available for reference and study. I further agree that permission for extensive copying of this thesis for scholarly purposes may be granted by the head of my department or by his or her representatives. It is understood that copying or publication of this thesis for financial gain shall not be allowed without my written permission.

Department of Physics & Astronomy

The University of British Columbia
Vancouver, Canada

Date Mar-12-1997

Abstract

An important question with respect to radiation therapy is to what degree of accuracy, dose delivery can be achieved in clinical practice. It is well understood that accurate delivery of a specific radiation dose to a target volume is critical to the success of radiation therapy.

The use of portal imaging in radiotherapy for verification of field size, shape, orientation and patient setup is of vital importance in delivering successful radiation treatment. One of the modalities used in improving tumor localization and geometric verification of field sizes is the on-line electronic portal imaging device (EPID).

In this thesis, the dosimetric characteristics of a scanning liquid-filled ionization chamber electronic portal imaging device (SLIC-EPID) have been investigated. To assess the system's response in relation to radiation beam intensity, a series of characteristic curves were obtained for various field sizes and energies. It was shown that the response of the imaging system was dependent on incident radiation intensity and could be characterized by a square root function to within 1% accuracy.

Exit dose measurements with the SLIC-EPID on the central axis of the beam using homogeneous attenuating phantom materials revealed that the Portal Vision™ is capable of measuring the transmission dose to within 3% of standard dosimeters, such as the ionization chamber.

For dosimetry applications, additional build-up material on top of the detector cassette of the portal imager is required to calibrate the system prior to dose measurements. Open field and wedged dose profiles of the portal imager show an accuracy of better than 3.5% when compared with those obtained using an ionization chamber in regions near field edges.

SLIC-EPIDs, when configured appropriately have the potential of being used as exit dosimeters. They are capable of determining the relative dose at the exit surface of the patient with an accuracy of better than 3.5%.

Table of Contents

Abstract	ii
Table of Contents	iv
List of Figures	vii
List of Tables	x
List of Equations	xii
Acknowledgments.....	xiii
Chapter 1: Portal Imaging In Radiotherapy: An Introduction.....	1
1.1: Background	1
1.2: Portal Imaging Using Films	2
1.3: Drawbacks of Portal Films.....	4
1.4: Alternatives to Portal Films	5
1.5: Video-based Electronic Portal Imaging Devices (VEPIDs).....	7
1.6: Advantages and Drawbacks of VEPIDs.....	10
1.7: Scanning Liquid-filled Ionization Chamber Electron Portal Imaging Devices (SLIC-EPIDs)	12
1.7.1: <i>Image Detector</i>	12
1.7.2: <i>Scanning Modes</i>	14
1.7.3: <i>System Calibration</i>	14
1.8: Justification for EPIDs in Radiotherapy	20
1.9: Thesis Overview	21

Chapter 2: Theory and Experimental Materials	23
Part I: Theory	23
2.1: Interaction of Radiation with Matter: Mechanism of X-ray Production ...	23
.....	23
2.1.1: <i>Inelastic Collision with Nuclei: Bremsstrahlung Production ..</i>	23
2.1.2: <i>Inelastic Collision with Atomic Electrons: Characteristic</i>	
<i>Radiation Production</i>	24
2.2: The Compton Interaction	26
2.3: Measurements of Absorbed Dose	28
2.3.1: <i>Electronic Equilibrium</i>	28
2.3.2: <i>Bragg Gray Cavity Theory</i>	30
Part II: Experimental Materials	33
2.4: The Medical Linear Accelerator (linac)	33
2.4.1: <i>Major Components of a linac</i>	34
2.5: Linac accessories.....	40
2.5.1: <i>Wedge Filters</i>	40
2.6: Radiation Dosimeters.....	43
2.6.1: <i>Farmer-type Air Ionization Chamber.....</i>	43
2.6.2: <i>Thermoluminescent Dosimetry (TLD).....</i>	46
2.6.3: <i>Semiconductor Detectors</i>	48
2.7: Wellhofer (WP700) Water Tank System	48
 Chapter 3: Characteristic Curves of SLIC-EPID	 51
3.1: Experimental Methods	51
3.2: Results.....	53
3.3: Discussion	59
 Chapter 4: Transmission Dose Measurements.....	 61
4.1: Experimental Methods	61
4.2: Results.....	63

4.2.1: <i>Perspex Phantom</i>	63
4.2.2: <i>Aluminum Phantom</i>	67
4.2.3: <i>Lead Phantom</i>	69
4.3: Discussion	71
Chapter 5: Portal Dose Profiles	73
5.1: Introduction	73
5.2: Experimental Methods	77
5.2.1: <i>Calibration of SLIC with Build-up Material</i>	77
5.2.2: <i>Wedge Dose Profiles</i>	79
5.3: Results	80
5.4: Discussion	85
Chapter: 6: Conclusions	87
6.1: Summary	87
6.2: Future Work	91
References	92
Appendix 1: C-Code for analysis of portal imager output data	97

List of Figures

Figure 1.1: Cross sectional diagram showing the formation of an image in portal films	3
Figure 1.2: Schematic diagram of fluoroscopic system	9
Figure 1.3: Schematic diagram of a fiber optic fluoroscopic electronic portal imaging device	11
Figure 1.4: Schematic diagram of a liquid-filled ionization chamber imaging system	13
Figure 1.5: A flood field image taken by the SLIC.....	17
Figure 1.6: A dark field image taken by the SLIC-EPID	18
Figure 1.7: Images of head and neck taken by the SLIC-EPID and a simulator	19
Figure 2.1: The graphical representation of bremsstrahlung and the characteristic radiation processes	25
Figure 2.2: The graphical representation of Compton effect	27
Figure 2.3: Graph showing increase in absorbed dose with depth in the build up region.	29
Figure 2.4: Schematic diagram of a high energy radiotherapy linac	37
Figure 2.5: Schematic diagram of the linac's head	39
Figure 2.6: Schematic diagram of wedge filters and isodose distributions.....	42

Figure 2.7: Schematic diagram of a Farmer-type ionization chamber (0.06 cc, PTW)	45
Figure 2.8: Energy level diagram illustrating the thermoluminescence process.....	47
Figure 2.9: Cross sectional view of the Wellhofer dosimetry system.....	50
Figure 3.1: The schematic diagram of the system set-up for determination of characteristic curves.....	52
Figure 3.2: Characteristic curves for the 6 and 10 MV beams for a 5x5 cm ² radiation field size	54
Figure 3.3: Characteristic curves for the 6 and 10 MV beams for a 10x10 cm ² radiation field size.....	55
Figure 3.4: Characteristic curves for the 6 and 10 MV beams for a 20x20 cm ² radiation field size.....	56
Figure 3.5: Superposition of characteristic curves for three field sizes	58
Figure 4.1: Schematic diagram of the geometry for the relative exit dose measurements.	62
Figure 4.2: Transmission dose measurements for perspex	66
Figure 4.3: Transmission dose measurements for aluminum.....	68
Figure 4.4: Transmission dose measurements for lead	70
Figure 5.1: The cross-plane dose profiles measured with an ionization chamber at various depths in water	75
Figure 5.2: Cross section of system set-up for the calibration of the SLIC	78

Figure 5.3: Open field and wedged dose profiles of the SLIC in imaging and dosimetric modes and their comparison to ionization chamber profiles for 6 MV beam.....81

Figure 5.4: Open field and wedged dose profiles of the SLIC in imaging and dosimetric modes and their comparison to ionization chamber profiles for 10 MV beam.....82

List of Tables

Table 3.2.1: Parameters P_1 and P_2 of the square root function used in the determination of dose response characteristic curves.....	57
Table 4.1.1: Physical properties of phantom materials used in transmission dose measurements.....	63
Table 4.2.1.1: The maximum deviations in the response of the SLIC-EPID from that of a calibrated ionization chamber for transmission measurements through perspex.....	65
Table 4.2.2.1: The maximum deviations in the response of the SLIC-EPID from that of a calibrated ionization chamber for transmission measurements through aluminum.....	67
Table 4.2.3.1: The maximum deviations in the response of the SLIC-EPID from that of a calibrated ionization chamber for transmission measurements through lead	69
Table 5.1.1: The variation in dose measured by an ionization chamber at the central axis of the beam and the field edges for various depths in water	76
Table 5.3.1: The maximum percentage deviations of dose profiles on central axis of the beam between the SLIC-EPID in DM and ion chamber for various field sizes and energies	83
Table 5.3.2: The comparison of measured dose profiles at field edges (3 cm from the central axis) between the SLIC-EPID and ion chamber for a collimated field size of 5x5 cm ² and various energies.....	83

Table 5.3.3: The comparison of measured dose profiles at field edges (6 cm from the central axis) between the SLIC-EPID and ion chamber for a collimated field size of $10 \times 10 \text{ cm}^2$ and various energies.....84

Table 5.3.4: The comparison of measured dose profiles at field edges (10 cm from the central axis) between the SLIC-EPID and ion chamber for a collimated field size of $15 \times 15 \text{ cm}^2$ and various energies.....84

List of Equations

Eqn. 2-1: Energy of ejected electron in Compton process	26
Eqn. 2-2: Energy of scattered photon in Compton process	26
Eqn. 2-3: The energy absorbed in a medium	30
Eqn. 2-4: Dose absorbed in small mass of tissue	31
Eqn. 2-5: Calibration factor, N_{gas}	32
Eqn. 2-6: Absorbed dose for any energy	33
Eqn. 2-7: Wavelength of a power source in linacs.....	34
Eqn. 3-1: Pixel values of the SLIC-EPID characterized by a square root model.....	53
Eqn. 3-2: Electrometer reading derived from the square root function	53
Eqn. 4-1: Electrometer reading derived from the square root model.....	64
Eqn. 4-2: Calculated transmission ratio determined from the square root model.....	64
Eqn. 5-1: Calculation of field flatness	74

Acknowledgments

I would like to take this opportunity to express my gratitude to those who made this research an excellent learning experience for me. My most sincere thanks go to my Supervisor, Dr. Ellen El-Khatib, to whom I am deeply indebted for her guidance, assistance and invaluable advice throughout this work.

Thanks are also due to Dr. Rasika Rajapakshe for his co-supervision in this project.

I wish to express my appreciation to physicists; Dr. Sherali Hussein, William Kwa, Dr. Mick Nikolic, Larry Watts, Dr. Cynthia Araujo, Dr. Ingrid Spadinger, Dr. Cheryl Duzenli, Greg Kennelly, Bob Harrison, and Dr. Chantal Audet for being very approachable and sharing their knowledge with me.

Hats off to the electronics crew; Rodger Sabey, Randy Wick, Denny Yu, and Don Melsness for their patience and for always taking the time out of their schedule to teach me the “*secrets*” of the portal imager and linac 2. Thanks are also due to physics assistants; Vince Strgar and John Wolters for always working around their schedule to accommodate students.

And of course who could forget the machine shop crew; Colin Potter, and Michel Rocher whom I could always rely on, when it came to making state of the art phantoms with last minute requests. Many thanks to both of them.

Special appreciation is due to my family, in particular, my parents, for their continuous love, encouragement and understanding throughout all the years that I have been away from home.

I would like to dedicate this work to the memory of my brother, Mehran.

H. Parsaei, Spring of 1997.

Chapter 1

Portal Imaging In Radiotherapy: An Introduction

1.1 Background

The role of radiation therapy in treating carcinogenic tumors is to deliver an adequate dose of ionizing radiation to the tumor site while minimizing the risk of severe damage to surrounding healthy tissues. A key factor in delivering the correct radiation absorbed dose is the ability to reproduce the individual patient's daily irradiation geometry over a large number of dose fractions. Therefore, geometric accuracy has a very vital role in successful radiation therapy.^{1,2}

While substantial improvements have been made over the last few years in linear accelerator technology³, quality control, and treatment planning, little attention has been focused on radiation field placement errors. These errors involve displacement of radiation fields due to organ movements or shifting skin, weight loss, patient movement during or between the sessions, incorrect beam alignments and improper placement of shielding blocks. Several studies^{4,5,6} have shown that the localization errors can significantly be reduced by using portal films.

1.2 Portal Imaging Using Films

Traditionally, geometric verification of radiation fields is accomplished by comparing the original treatment simulation radiograph [Fig. 1.7b], an image taken with low energy radiation (kilovoltage range), to a portal radiograph [Fig. 1.7a], an image taken with high energy radiation (megavoltage range), both placed directly under the patient.

The American Association of Physicists in Medicine (AAPM) in a report distinguishes two types of portal images.⁷ These are *verification* and *localization* portal films, where a verification film is a portal radiograph produced when the image receptor is exposed to the entire treatment delivered with the field, whereas a localization film is a radiograph produced by an exposure which is short compared to the daily treatment time required for that treatment field.

The portal film images are not directly formed from the incident primary photons exiting the patient, but rather from Compton recoil electrons produced by the primary photons in the vicinity of the radiographic film. The process of image formation may be described schematically with the help of Fig. 1.1. When portal films are used for treatment field verification, a close screen contact (metal screen made of copper or lead) is required to absorb the shower of the scattered electrons emanating from the exit surface of the patient (solid arrows). Scattered electrons do not carry useful patient information. In fact they increase the blur in the image.⁷ The photons (shown by dots) transmitted through the patient produce Compton recoil electrons in the screen and their emission from the screen will be an indication of anatomical structures which appear on the film. An appropriate

choice of film and screen thickness are of vital importance to image quality. The most important image quality parameters in portal imaging are image contrast and spatial resolution. Image contrast is defined as the difference in density existing between various regions of the image and spatial resolution of an image is the ability to display, as separate images, two objects that are very close to each other on an image.

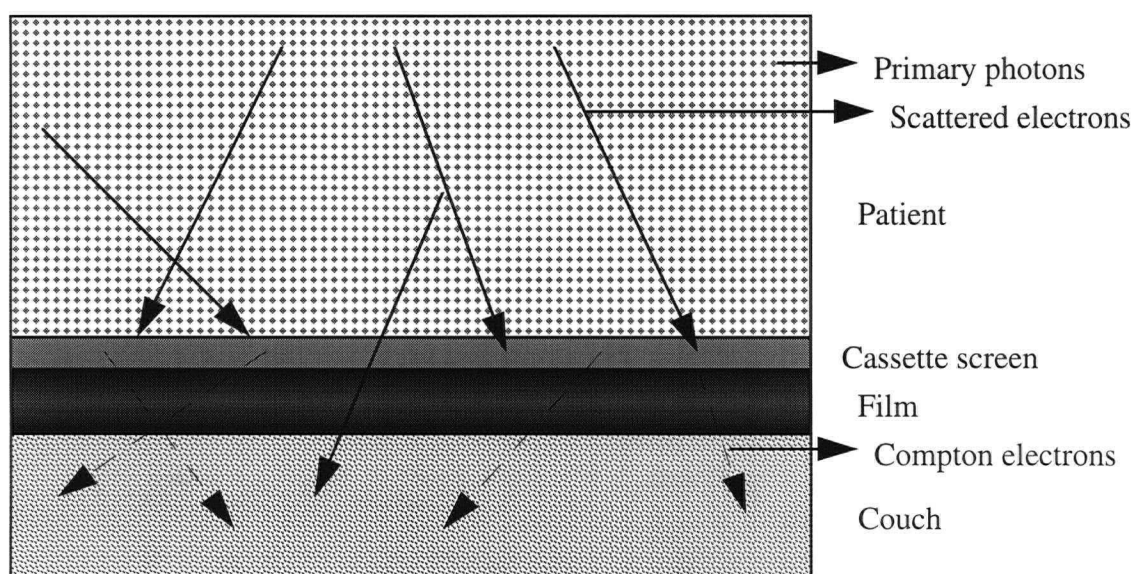


Figure 1.1: Cross sectional diagram showing the image formation in portal films. The cassette screen absorbs the shower of scattered electrons (solid arrows) from the patient which will otherwise decrease the contrast. Photons (shown by dots in the patient) incident upon screen will cause emission of Compton electrons (dashed arrows) which in turn are responsible for the formation of the radiographic image.

Differences in image quality between portal radiographs are produced with differences in metal screens used.⁷ An increase in screen thickness has some disadvantages and advantages. Thicker screens will reduce resolution, since electrons originating within the screen now can reach the film from more distant points and scatter laterally in the process, causing blurring of the image. On the other hand, when the thickness of the screen is reduced, the image resolution may improve, however, the electrons emanating from the patient may reach the screen and lower the image contrast as a result. Hence, depending on the desired image quality and what should be seen clearly in the radiographic image, the contrast or spatial resolution of the image can be varied by altering the screen thickness of the portal film.

Although advances have been made to improve the quality of portal films, they still suffer from a number of drawbacks that restrict their usefulness as an interactive tool in the quality control of radiotherapy.^{4,8} These are discussed in the following section.

1.3 Drawbacks of Portal Films

The image quality of portal films is in general not very good.⁷ This is because of the effects of photon attenuation and absorption at the higher photon energy in the megavoltage range (MV) relative to the diagnostic kilovoltage range (KV). As the energy is increased from the low to the higher range (2 MeV and up), the probability of photoelectric interactions which have a high atomic number dependence reduces to nil and

therefore image contrast is degraded. These and other drawbacks of portal films are summarized as follows.^{7,9,10}

1. Low contrast images due to the predominance of Compton scattering in the megavoltage energy range. Also the higher energy photons produce low resolution images.
2. Portal films have to be developed before images are available and do not allow immediate feedback before a complete dose fraction is delivered. Furthermore, irradiation has to be interrupted for film removal and processing. Consequently the results can only be taken into account for the next patient setup.
3. Portal films usually have a different magnification factor than the simulator or reference films obtained at diagnostic kilovoltage energies. Therefore, corresponding dimensions have to be estimated or measured by a ruler which is not very accurate.
4. The high cost of portal films and time limitations are other factors which may be considered as a drawback.

Therefore, alternative methods have been investigated and implemented to replace portal films.¹¹

1.4 Alternatives to Portal Films

Improvements in field verification using portal films have contributed to greatly reducing the geometric inaccuracies in radiation field placement,^{5,12,13} however, the verification that treatments are delivered with the same degree of precision on a daily basis

over an entire course of radiation therapy is not practical using conventional portal films. In addition, it is believed that there is more information contained in the radiation beam than is presently extracted from portal films.¹⁴ These considerations have generated an interest in the development of on-line electronic portal imaging devices. Over the last few years each of the major manufacturers of medical linear accelerators (Varian Associates™, Siemens Medical Systems™, General Electric™, and Philips Medical Systems™) have offered electronic portal imaging devices (EPIDs) as part of their systems. Therefore, on line electronic portal imaging devices are coming into clinical service in support of radiotherapy as an alternative to conventional portal film imaging.

EPIDs are designed to extract as much information as possible from a given radiation beam.¹⁵ A wide variety of techniques have been developed to acquire images at real or near-real time.¹¹ In this chapter two of these designs, which are commercially available are described, namely;

1. The Fluoroscopic or Video-based Electronic Portal Imaging Devices (VEPIDs), and
2. The Matrix of Scanning Liquid-filled Ionization Chamber Electronic Portal Imaging Devices (SLIC-EPIDs).

1.5 Video-based Electronic Portal Imaging Devices (VEPIDs)

Siemens Medical Systems™, Philips™ Inc., and General Electric™ manufacture on-line portal imaging systems based on a fluoroscopic approach. A schematic diagram of this device is shown in Fig. 1.2. It consists of a metal screen in combination with a phosphor screen acting as an electron to visible light converter, a front surface mirror angled at 45 degrees, and a video camera.

The metal plate, 1 to 2 mm in thickness, acts as the x-ray detector by first transferring part of the energy of the impinging photons to secondary electrons through mostly Compton effect. The secondary electrons then in turn interact with the fluorescent screen, bonded to the metal sheet, which gives out light via de-excitation. The image of the anatomical structure is then reflected by the front surface mirror angled at 45 degrees and captured with a video camera which is interfaced to a host computer for image digitization, processing and storage.^{16,17}

All fluoroscopic systems are in general efficient as data can be collected for image formation at near-real time (~ 2 sec.). However, the optical image is greatly de-magnified when large field images are focused on to a small area on the video camera target. As a result, less than 0.05% of the secondary light photons are collected for image formation.⁹

The quality of the fluoroscopic image is dependent on the number of high energy photons detected per unit area. Therefore, depending on the image quality desired, one can either increase the spatial resolution or increase image contrast. For example, at the expense of

some loss in resolution due to the scattering of secondary electrons and light photons, thicker fluorescent screens have been used to increase the light photon intensity.⁹

Although VEPIDs are superior to portal films, they do not satisfy all the requirements in a clinical setting.

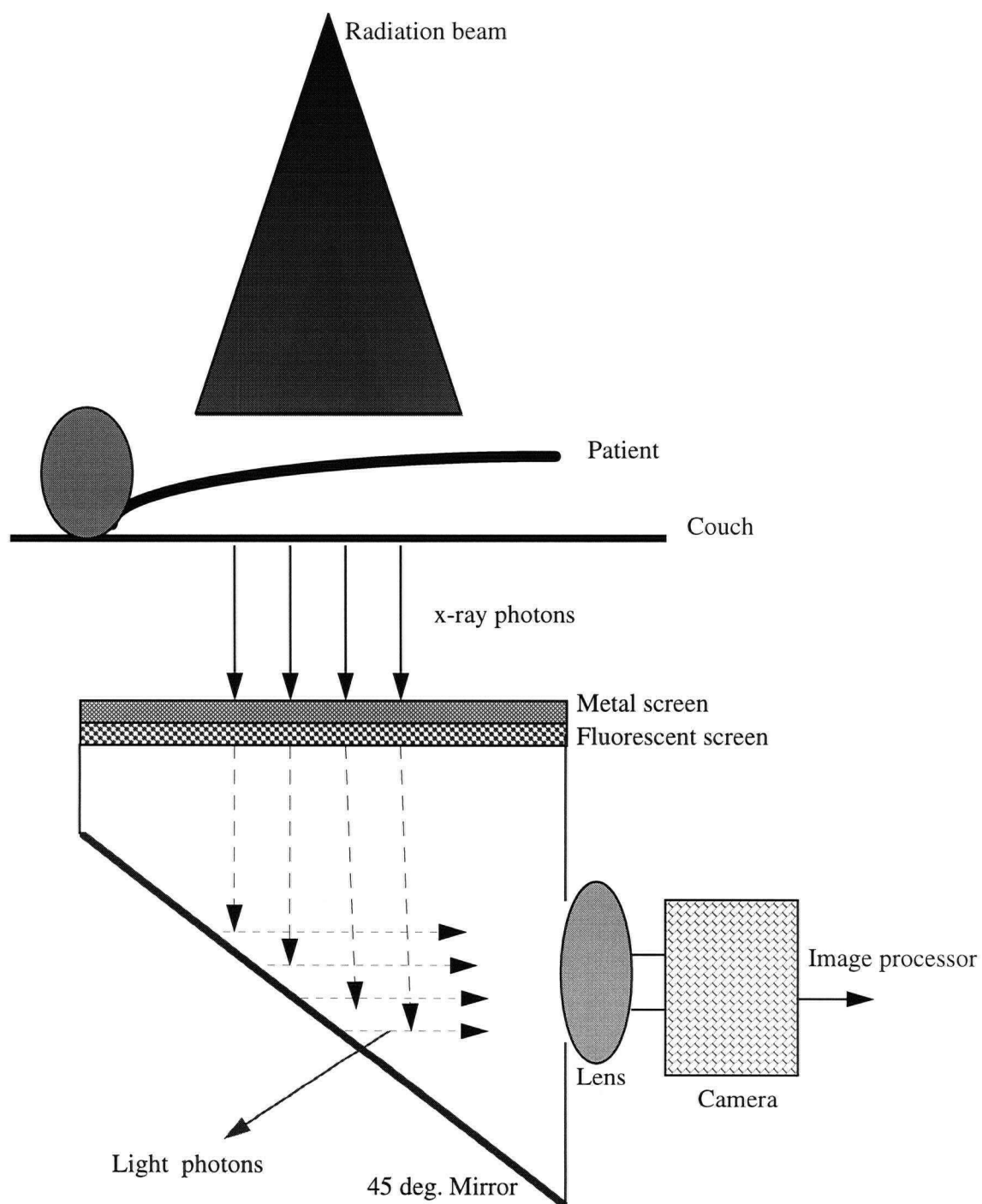


Figure 1.2: Schematic diagram and the main components of a fluoroscopic system. The video camera is coupled to a frame grabber for image acquisition.

1.6 Advantages and Drawbacks of VEPIDs

Despite the inefficiency of the video based system in collecting the secondary light photons, the fluoroscopic systems are in general fast in image acquisition. The major advantages of these systems are their ease of assembly and the speed in which an image is acquired. A portal image can be displayed in less than two seconds after the beam is turned on, which allows rapid on line treatment verification. Although the fluoroscopic systems are superior to portal films, there are a number of drawbacks associated with these systems. Some of which are;¹⁸

1. The data is typically digitized with an 8 bit frame grabber and therefore have less contrast information than scanning systems.
2. Non-uniformity of the lens in light collection would also limit the dynamic range of the system.
3. A major drawback of these systems is in the bulkiness of the 45° mirror housing which is typically about 40 cm tall. Mechanical modifications can be made to provide a housing that is retractable, or detachable, so as to save work space.
4. Mirror based imaging systems cannot be used on therapy units with beam stoppers.

A fluoroscopic system shown in Fig. 1.3 was developed by Wong *et al*,^{16,17} based on fiber optic image reducers with the intent of replacing the bulky mirror assembly and the camera lens. The system holds an array of 16x16 image reducer bundles. Each bundle in turn contains 16x16 plastic optical fibers with an input area of 1.5 mm by 1.5 mm for each

fiber. Therefore within a height of 12 cm, a $40 \times 40 \text{ cm}^2$ input image area can be reduced to a $2.5 \times 2.5 \text{ cm}$ output image. However, these systems are not available commercially.

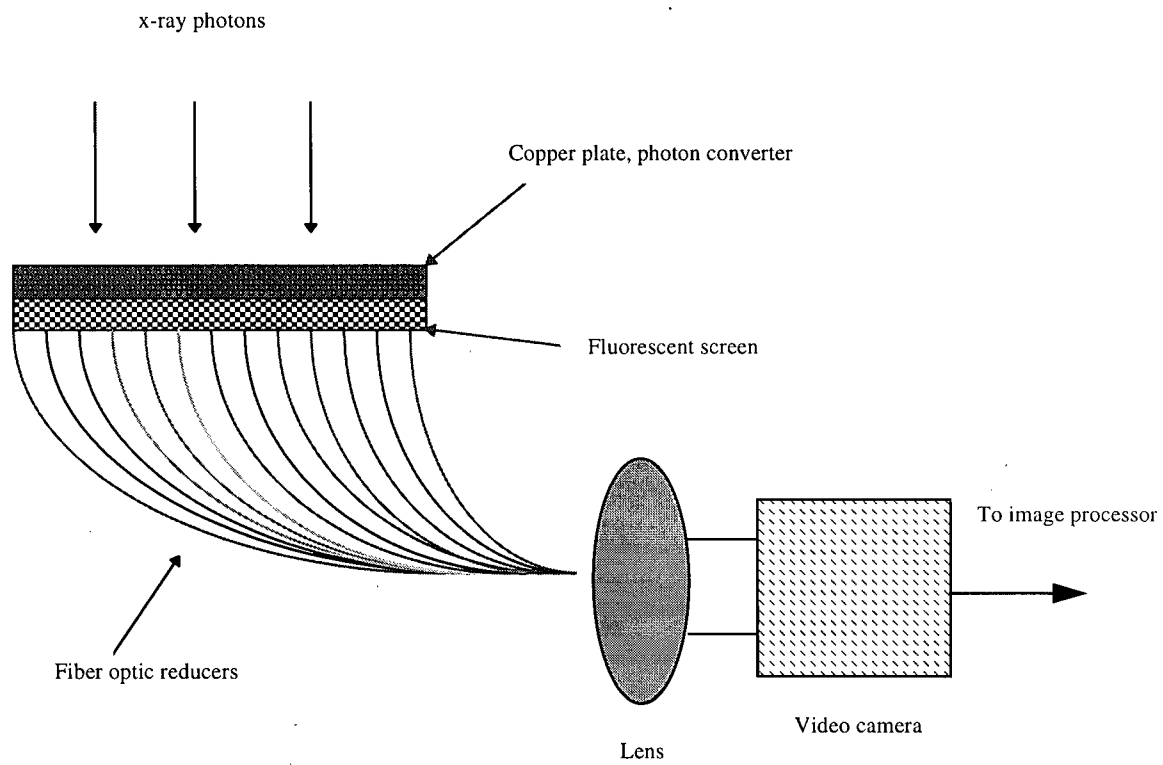


Figure 1.3: Schematic diagram of a fiber optic fluoroscopic electronic portal imaging device.

1.7 Scanning Liquid-filled Ionization Chamber Electron Portal Imaging Devices (SLIC-EPIDs)

The matrix of Scanning Liquid-filled Ionization Chamber (SLIC-EPID) shown in Fig. 1.4, was originally developed in the Netherlands and marketed by Varian Associates™ under the name of Portal Vision™. This is the detector used in this investigation.

1.7.1 Image Detector

The image detector is essentially a matrix of 256 x 256 straight wire electrodes enclosed in a chamber filled with ionizing liquid. Iso-octane is used as the ionization medium. The physical size of each chamber is 1.27x1.27x1 mm³. The detector measures 32.5x32.5 cm² across the image capture area. It has the shape of a standard film housed in a lightweight (~ 7 kg) portable cassette. The ion chambers along with the electronics of the detector are protected by a casing which is made of thermoplastic material. With exposure to radiation for long periods of time, a gradual loss of physical strength of the casing of the detector is expected.¹¹

The detector used in this study is mounted on a Varian Clinac™ 2100C/D linear accelerator and can be retracted when not in clinical use. Both arms of the imaging system have motorized vertical movement, ranging from 110-170 cm from the radiation source of the linac when in clinical mode. This wide range of movements allows the positioning of the portal imager close to the patient to obtain the maximum field of view (FOV) and

optimized image quality. Fig. 1.4 illustrates in block diagram the matrix of ionization chambers and associated circuitry.

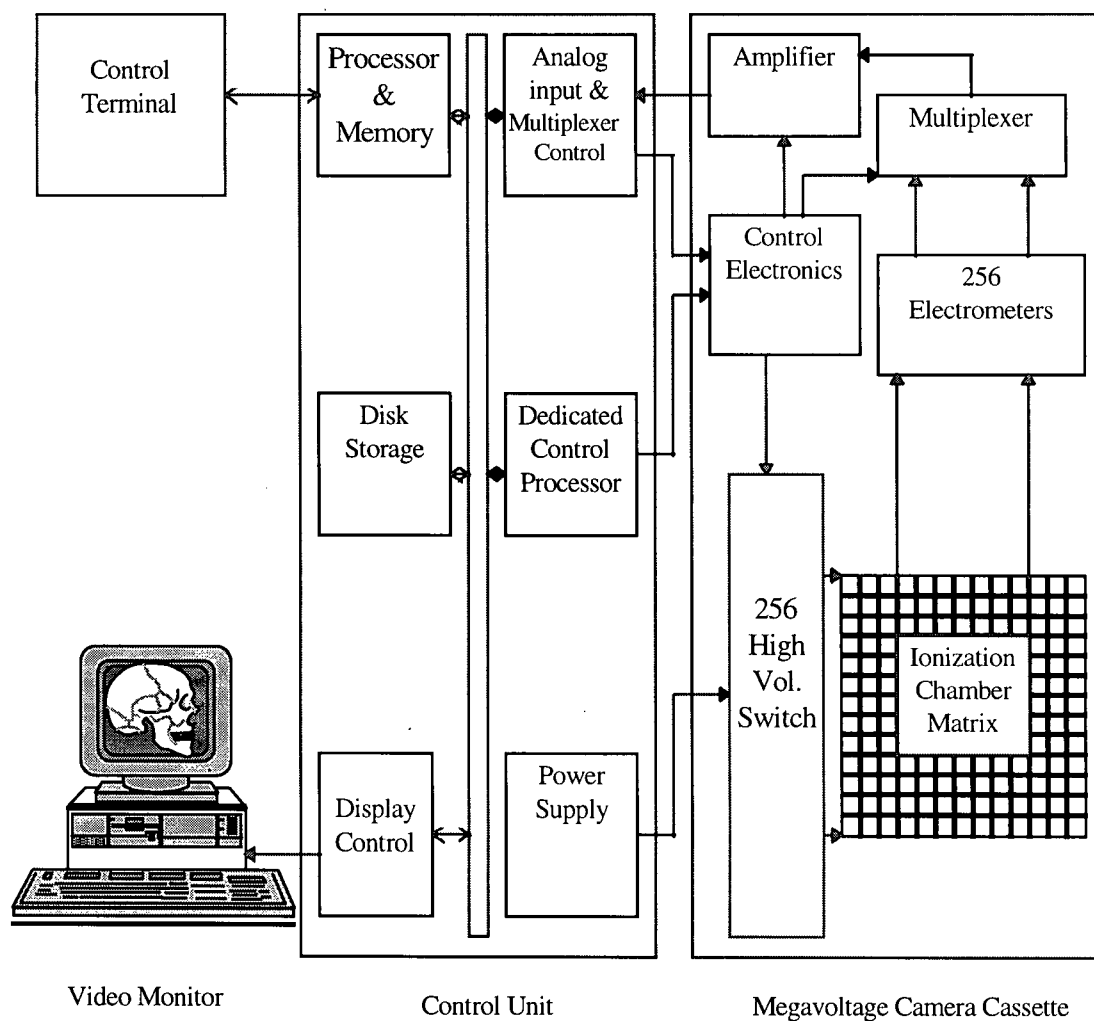


Figure 1.4: Schematic diagram of a liquid-filled ionization chamber imaging system. The matrix of chambers has two sets of perpendicularly oriented electrodes separated by a 1-mm fluid filled gap. The strip electrodes are effectively scanned by sequentially activating the perpendicular high voltage electrodes. The matrix has a sensitive area of $32.5 \times 32.5 \text{ cm}^2$.

To acquire an image,^{11,19,20} the ionization matrix is scanned row by row, by successively switching high voltage electrodes and measuring the very small ionization current in all 256 column electrodes thus forming an image of more than 65,000 pixels. The ionization chamber operates at a polarizing voltage of 300 volts, which is well below saturation for the ionizing liquid.

1.7.2 Scanning Modes

Two types of sampling or scanning modes are available in the Portal Vision™ systems; standard and fast. In the standard sampling mode, all the 256 high voltage rows are activated sequentially [Fig. 1.4], yielding the highest resolution but a longer acquisition time. In the fast sampling mode, every other high voltage line is activated simultaneously, yielding a shorter acquisition time but at a reduced resolution. The nominal acquisition time for the standard sampling mode ranges from 5 to 9 seconds, whereas the nominal sampling time for fast scanning mode ranges from 1.5 to 5 seconds.²¹

1.7.3 System Calibration

Calibrating the ion chambers of the imaging device is necessary to prevent artifacts that may arise during switching of the high voltage electrodes. It can also correct for individual ion chamber sensitivity. Sources of sensitivity variation between individual ionization chambers may be;¹⁹ (1) electrode shape differences, (2) electrode surface inhomogeneities, and (3) most importantly the sensitivity of the ionization chambers

depends on the local thickness of the liquid layer in the ion chamber. System calibration also corrects for electrometer offsets which are caused by scattered radiation and instability in temperature due to overheating of electronics.

Calibration of the detector is usually performed once every two weeks. The detector cassette is positioned at a fixed distance, typically 150 cm from the radiation source of the linac and the radiation field size is set to cover the sensitive area of the imaging device. The calibration is then performed in two steps.

1. Individual ion chamber offset values are measured by acquiring images without the radiation beam on. This is referred to as "*Dark field irradiation*". This image will take into account the background radiation due to the electronic circuitry of the linac.
2. The sensitivity of each ionization chamber is measured by acquiring images with the radiation beam on. This is referred to as the "*Flood or flat field irradiation*".

The subsequent clinical images are then calculated by the imaging software based on the average of dark field and flood field images as well as electrometer offsets for each image.

It should be emphasized that the pixel values in the portal imager output files are not the raw pixel values but, are numbers after software corrections are applied to remove background radiation and to correct for individual pixel sensitivity.^{15,19}

Figures 1.5 and 1.6 illustrate examples of flood field and dark field images respectively taken by the imaging system using 6 MV photons. The images are taken with the system set on standard sampling mode to ensure charge collection from all the 65536 ion chambers. Dark bands on the flood field image are mainly due to artifacts created by

sequentially switching the high voltage electrodes. The vertical bands on the dark field image in Fig. 1.6 show the variations in individual electrometer offsets.¹⁹

Figure 1.7a illustrates an example of a portal image acquired by the system and in Fig. 1.7b is shown the corresponding simulator image. The comparison of the images clearly demonstrate the difference in contrast at the two energies.

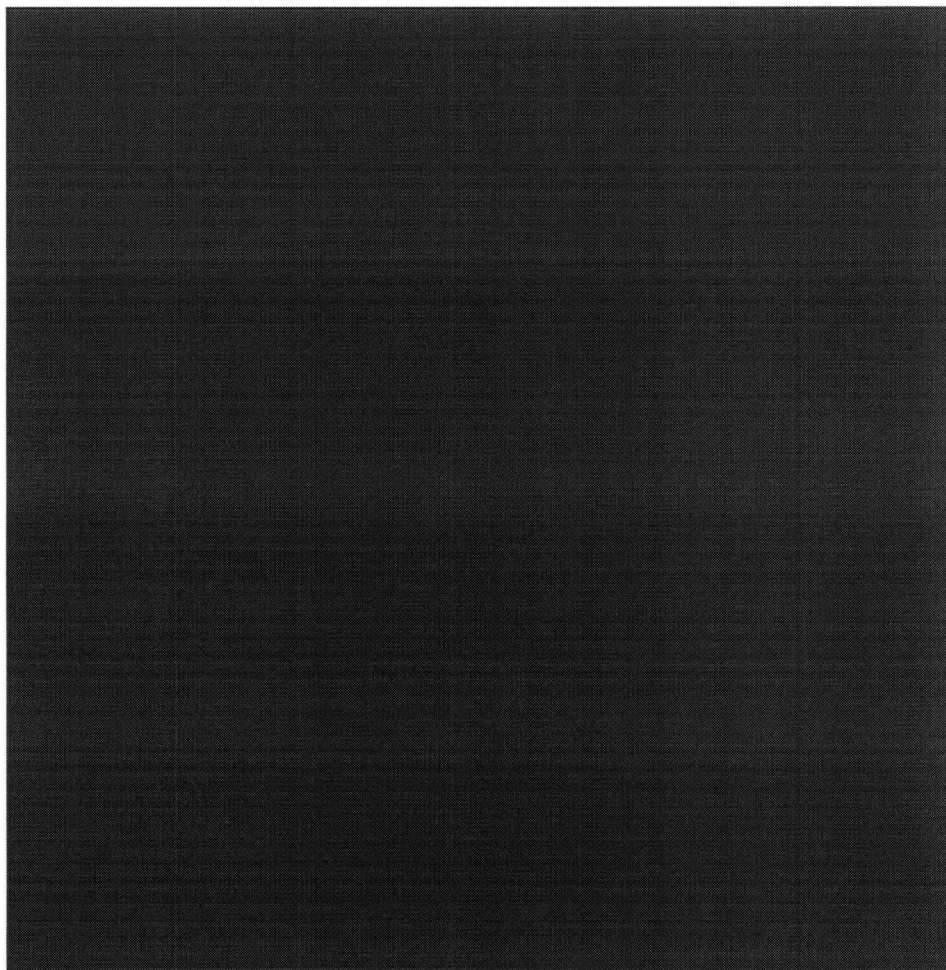


Figure 1.5: Flood field image taken by SLIC-EPID using a 6 MV beam. Source to detector distance, SDD, was set at 150 cm with a field size of $32 \times 32 \text{ cm}^2$ at detector level and standard sampling mode.

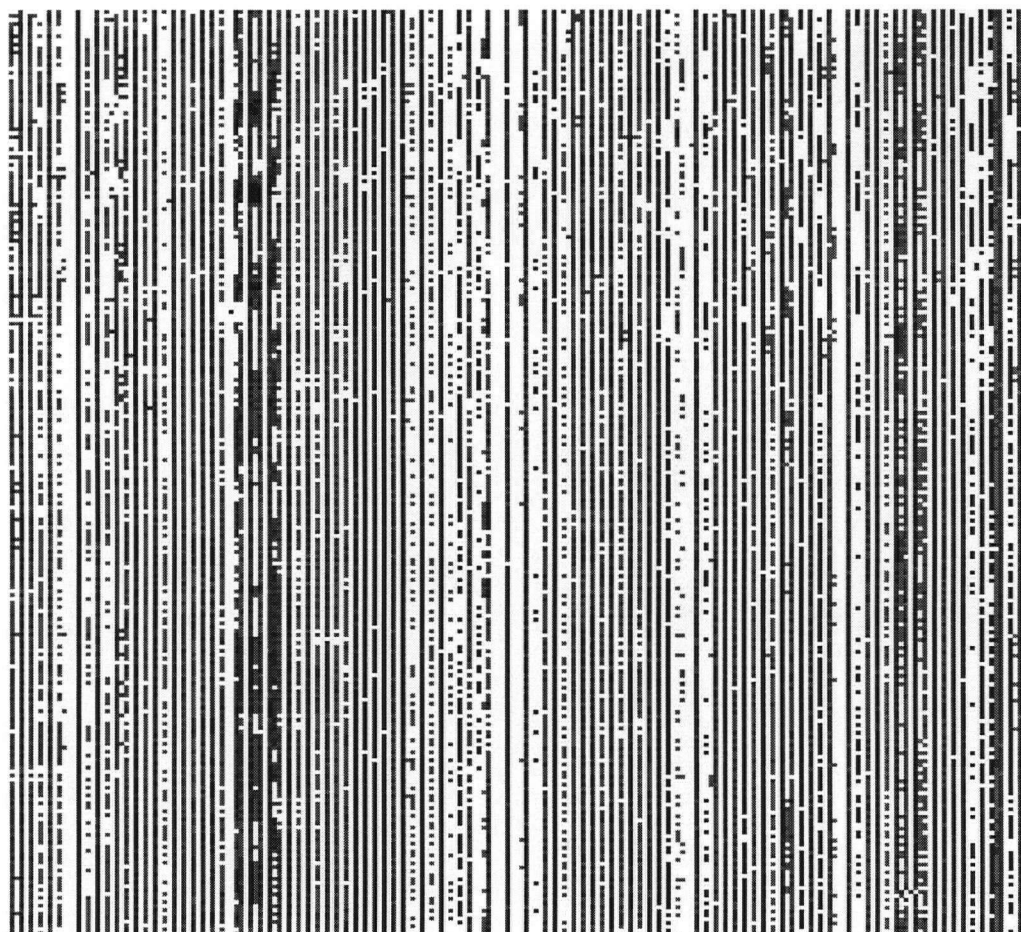
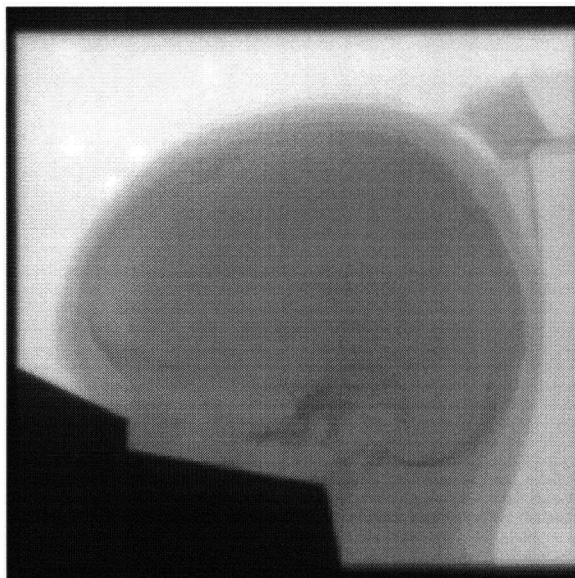


Figure 1.6: Dark field image taken by SLIC-EPID with no beam. Source to detector distance, SDD, was set at 150 cm with a field size of $32 \times 32 \text{ cm}^2$ at the detector level and standard sampling mode.

(a)



(b)

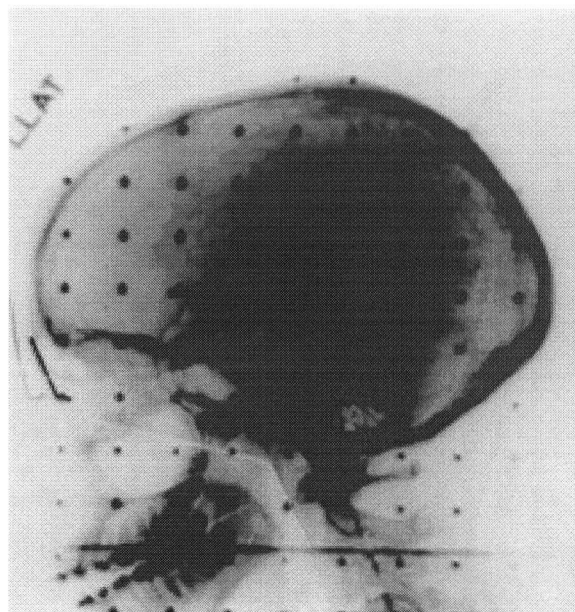


Figure 1.7: Images of the head and neck. Taken (a) by a SLIC-EPID and (b) the corresponding reference image taken by a simulator for the purpose of comparison.

1.8 Justification for EPIDs in Radiotherapy

EPIDs are rapidly establishing a reputation for producing high quality portal verification and localization images.¹¹ Their inherent spatial resolution and image manipulation capability mean that they can be used to measure and analyze field placement errors very easily before a large portion of the dose is administered to the patient.²² This in turn can put the treatment operator in a position to instantly compare the reference image to that of the actual treatment field and correct for any variations seen in the treatment field.

Dynamic Conformal Therapy, a technique in which the radiation field is conformed to the shape of the treatment volume as the radiation beam is rotated around the patient requires real-time field verification.²³ This is because the tighter the dose distribution conforms to the target volume, the more serious patient mispositioning in the treatment fields become.²⁴ Therefore, to improve the quality of dose delivery, on-line electronic portal imaging devices have become the ideal tool for this task as near-real time images allow the treatment operators the intervention and intelligent use of data.

Although EPIDs are primarily used for assessing patient positioning and beam alignment,¹¹ they can be used to obtain quantitative information about delivered dose, beam flatness, and beam symmetry.

1.9 Thesis Overview

The dosimetric characteristics of a matrix of scanning liquid-filled ionization chambers mounted on a Clinac™ 2100C/D at our institute are studied under various conditions and its limitations and versatility are examined. The contents of this thesis consist of the following:

In Chapter 1, a brief overview of electronic portal imaging devices is given, in particular the video based system, SLIC, the device used in this work, and their close counterpart, the portal films. A detailed description of SLIC calibration is also given and its influence on image quality is discussed. Chapter 2 is divided into two parts; Part I describes the theoretical background relevant to this work and radiotherapy physics. In particular, the concepts of x-ray production, Compton interaction, radiation dosimetry, and calculation of absorbed dose are discussed. Part II focuses on experimental materials; the linac, wedge filters, various radiation dosimeters and the Wellhofer dosimetry water tank system. In Chapter 3 the characteristic curves of the SLIC are investigated as preliminary work required for the evaluation of the dosimetric properties of the system. The relationship between the incident radiation intensity on the detector and the output pixel values of the matrix of ion chambers is analyzed for 6 and 10 MV photon beams at various distances from the source and for several radiation field sizes.

The data collected by SLIC-EPID during image acquisition may be interpreted in other ways such that dosimetric information can be drawn from it.^{25,26} That is, the average pixel value within a region of interest (ROI) depends on the photon fluence at the corresponding

region of the detector. This in turn can be used to determine the intensity of the beam and consequently the dose at the exit surface of the patient.⁸ Exit dose measurements combined with entrance dose can be used as a basis for understanding the dose distribution within the patient and demonstrate possible deviations between the planned and measured doses which can result in recommendations for improved dose calculations.²⁷ Although, diodes and thermoluminescent dosimeters (TLDs) have been used in the determination of *in-vivo* entrance and exit doses, these dosimeters yield dose measurements at only a few points in the radiation field. Using portal imaging devices, the exit dose can be determined in the entire irradiation field,^{8,28} which in turn can provide better information about dose distribution in the patient. Therefore, in Chapter 4 the ability of the system to measure the relative exit dose at the central axis of the beam is studied for various homogeneous phantom materials. To assess the accuracy of these measurements, reference dose measurements are performed with a calibrated Farmer-type ionization chamber in combination with an electrometer at the same position.

In addition, exit dose measurements are determined at points off the central axis of the radiation beam. This is the focus of Chapter 5. In this chapter dose profiles obtained using the SLIC in a plane perpendicular to the central axis of the radiation beam for different energies and field sizes are studied. A series of open field and wedged dose profiles are obtained and compared to reference measurements done using an ionization chamber. Finally in Chapter 6, the results and conclusions of this investigation are summarized and future uses of EPIDs are briefly discussed.

Chapter 2

Theory and Experimental Materials

I. Theory

2.1 Interaction of Radiation with Matter: Mechanism of X-ray Production

X radiation is produced whenever a substance, commonly referred to as a target, is bombarded by high speed energetic electrons. There are two mechanisms by which x-rays are produced in a linear accelerator.²⁹ One is due to the radiative collisions of the high speed electrons with nuclei of target material and the resultant x-rays are known as *bremsstrahlung* x-rays. And the second type is *characteristic* x-rays, produced when energetic electrons collide with bound electrons.

2.1.1 Inelastic Collision With Nuclei: Bremsstrahlung Production

Bremsstrahlung occurs when energetic electrons are deflected from their path by the action of Coulomb forces of attraction as they pass in the vicinity of a nucleus. They lose part or all of their kinetic energy and by the conservation of energy, a quantum of

electromagnetic radiation is emitted into space [Fig. 2.1a]. The energy of the emitted quantum is equal to the reduction in kinetic energy of the decelerated electron.

Any one energetic electron may experience many interactions, each with reduced energy before being brought to rest within the target material. Therefore, the resulting bremsstrahlung photons may have a spectrum of energies, ranging from zero up to the maximum incident electron kinetic energy striking the target. Because of the production of a spectrum of energies of the bremsstrahlung photons, x-ray beams are given an energy unit of “MV”, where the mean energy of the bremsstrahlung spectrum is roughly one third of the maximum electron energy in MeV. For example, a 25 MeV monoenergetic electron beam impinging on a target will produce a 25 MV photon beam with a peak energy of 25 MeV and a mean energy of about 8 MeV.

2.1.2 Inelastic Collision with Atomic Electrons: Characteristic Radiation Production

Electrons incident on the target material may produce characteristic x-rays [Fig. 2.1b]. That is, an electron with energy E_0 , may collide with an orbital electron resulting in the ejection of the bound electron, leaving the atom ionized. The vacancy thus created in an inner shell is filled by transition of an electron from an outer shell. In so doing, the difference in binding energy of the two shells is radiated in the form of electromagnetic radiation with energy $h\nu$, and since the energy of the emitted x-ray is specific to the difference in binding energy of the two shells, it is referred to as characteristic radiation.

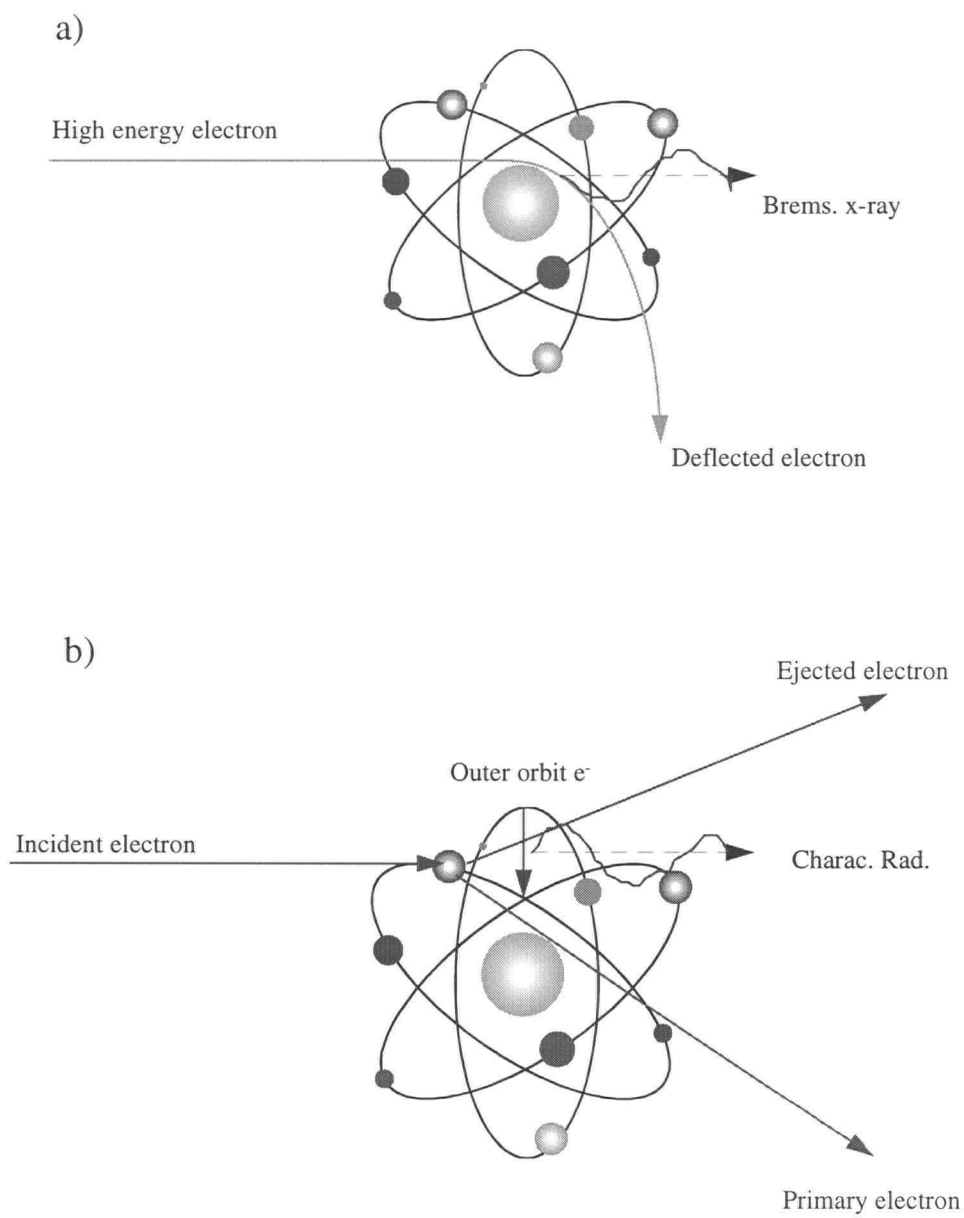


Figure 2.1: The graphical illustration of (a) bremsstrahlung process with deflected electron and the emerging photon and (b) characteristic x-ray production.

2.2 The Compton Interaction

In portal imaging using films, Compton electrons are responsible for formation of the radiographic image (Chapter 1). In the Compton process, the photon interacts with an atomic electron as though it were a “free” (*loosely bound*) electron. That is, the binding energy of the electron is much less than the energy of the bombarding photon. In this interaction, the electron receives some energy from the incoming photon and is ejected at an angle θ [Fig. 2.2]. The photon with reduced energy is then scattered with an angle ϕ . The process can be analyzed in terms of a collision between two particles, where the laws of conservation of momentum and energy can be applied to derive equations²⁹ (2-1) and (2-2), where $h\nu_0$ is the incident photon energy, $h\nu'$, is the scattered photon energy, and E is the energy of the recoil electron. m_0c^2 is the rest mass energy of the electron (0.511 MeV).

$$E = h\nu_0 \left[\frac{\frac{h\nu_0}{m_0c^2} (1 - \cos\phi)}{1 + \frac{h\nu_0}{m_0c^2} (1 - \cos\phi)} \right] \quad (2-1)$$

$$h\nu' = h\nu_0 \left[\frac{1}{1 + \frac{h\nu_0}{m_0c^2} (1 - \cos\phi)} \right] \quad (2-2)$$

The effective photon energy range in which the Compton effect is predominant in water and tissue like material is between 2 to 10 MeV.³⁰ It should be pointed out that since the

Compton process involves essentially the interaction of photons with free electrons in the absorbing material, the process is independent of atomic number Z . What this implies is that, if the energy of the beam is in the region where the Compton effect is the only mode of interaction, approximately the same attenuation of the beam will occur in any material of equal density thickness (gram/cm^2).

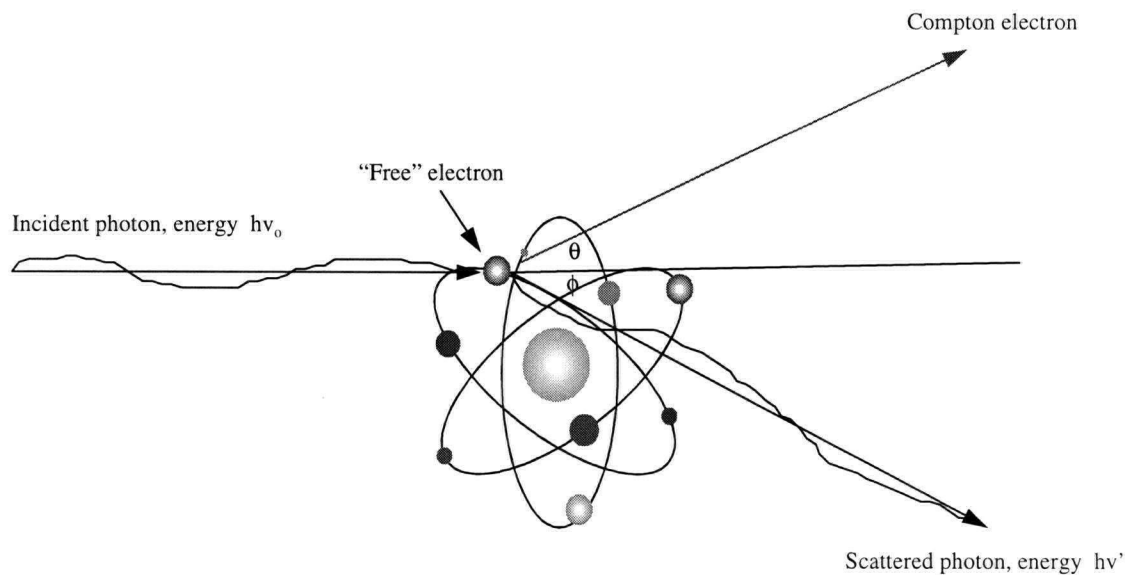


Figure 2.2: Diagram illustrating the Compton effect with the "free" electron emitted at an angle θ and incident photon scattered at an angle ϕ .

2.3 Measurements of Absorbed Dose

Prior to the discussion of dose calculation, the concept of electronic equilibrium must be introduced as it is an important consideration to the design of ionization chambers and dose calculation.

2.3.1 Electronic Equilibrium

Kerma (kinetic energy released in the medium), is calculated at a point at which photons from the incoming beam transfer all or part of their energy into the orbital electrons of the atoms in the medium. However, transfer of energy from the photon does not take place at the same location as the absorption of the energy by the medium. High energy electrons that are set in motion as the result of photon interactions may deposit their energy into the medium by either ionization or excitation losses at a remote distance from their point of departure. This has implications for the calculation of absorbed dose in a given medium.^{29,30,31}

For a small volume of medium placed in the path of x-ray photons, the electrons produced in the medium may or may not deposit all of their energy in the medium. That is, some electrons may gain enough energy so as to “*escape*” the volume in question. In addition electrons not produced in the volume may enter and deposit energy in it. Electronic equilibrium is said to occur if $(\text{Energy})_{\text{in}} = (\text{Energy})_{\text{out}}$, that is, the condition in which as many electrons are stopping as starting per unit mass is referred to as electronic

equilibrium. Fig. 2.3 illustrates a simplified schematic graph describing Kerma and absorbed dose in relation to electronic equilibrium. Region A in the graph is referred to as the build up region. In this region absorbed dose is increasing with depth. Region B, is the electronic equilibrium region, where as many electrons stop in any volume as are set in motion in it.

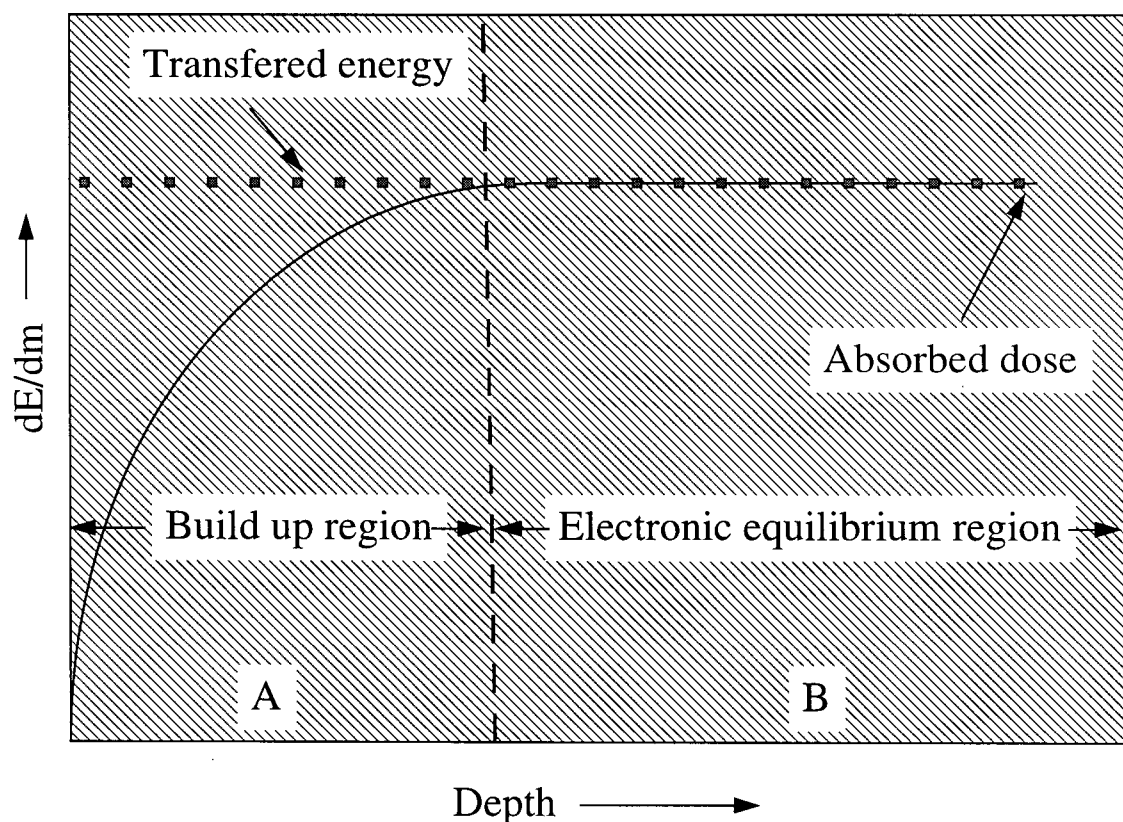


Figure 2.3: Graph showing increase in absorbed dose with depth in the build up region (A). Beyond the build up region is the region of electronic equilibrium where Kerma is equal to absorbed dose.

It should be noted that in this example it is assumed that there is no loss of primary photons due to attenuation. However, in practice, true electronic equilibrium is never established as no place in the medium are as many electrons set in motion as are brought to rest in it. And in this situation absorbed dose is always slightly higher than Kerma in region B.²⁹

2.3.2 Bragg Gray Cavity Theory

According to Bragg Gray theory, the ionization produced in a gas filled cavity placed in a medium is related to the energy absorbed in the surrounding medium. A condition of Bragg Gray cavity theory is that the cavity must be sufficiently small so that its introduction into the medium does not perturb the distribution of the electrons that exist in the medium without the cavity. Therefore the energy absorbed by the medium can be quantified by the following Bragg Gray relation and forms the basis for all dosimetry using ion chambers:^{29,30}

$$D_{med} = \frac{Q}{m_{gas}} W \left(\frac{\bar{S}}{\bar{S}} \right)_{gas}^{med} \quad (2-3)$$

Where D_{med} is the dose absorbed in the medium or the energy deposited per unit mass of the medium (E/m). Q/m_{gas} is the charge in Coulombs per unit mass of the gas in kg, W is the average energy required to produce one ion pair in the gas. Normally the gas used in ion chambers is air and its $W = 33.85$ Joules/Coulomb. \bar{S} is the ratio of average stopping

powers of the medium to that of the gas for the electrons crossing the cavity. $\bar{S} = \frac{1}{\rho} \frac{dE}{dx}$, is the mass stopping power and gives the energy loss per unit thickness measured in g/cm^2 . Therefore S is expressed in $\text{MeV cm}^2/\text{g}$. The units of absorbed dose are Joules/kg or Gray (Gy).

Absolute dosimetry using ion chambers is possible using equation (2-3). However, in practice an accurate determination of m_{gas} is difficult. This is because, although, in principle m_{gas} can be calculated from the volume of the chamber which can be determined accurately, in practice there are regions in the volume of the chamber that the electric field does not collect ions from and this portion of the chamber must not be included in the determination of m_{gas} . Therefore, most ion chamber dosimetry is based on a calibration factor, N_x (Roentgen/electrometer reading), traceable to a national standard lab. N_x , the exposure calibration factor, is derived from exposure, a quantity which is defined at a particular point in a beam of x-ray or γ -radiation as the ratio of Q/m , where Q is the total charge produced (of one sign) in a small volume of air of mass m . A unit which is still widely used for exposure even though no longer accepted as an SI unit is the Roentgen (R), ($1\text{R}=2.58 \times 10^{-4} \text{C/kg}$). In the presence of charged particle equilibrium (CPE), the dose in Gys to a small mass of tissue in air is given by:³⁰

$$D_{\text{med}} = X \cdot W_{\text{air}} \left(\frac{\mu_{\text{abs}}}{\rho} \right)_{\text{air}}^{\text{med}} \cdot A \quad (2-4)$$

Where X is the exposure in C/kg , that is, $X=M \cdot N_x$, where M is the electrometer reading, $W_{\text{air}}= 33.85 \text{ J/C}$, $(\mu_{\text{abs}}/\rho)_{\text{med}}/(\mu_{\text{abs}}/\rho)_{\text{air}}$ is the ratio of the mass absorption coefficient for

the medium to that in air. A , is an equilibrium thickness attenuation correction dependent on the energy fluence at the point of interest. It should be noted that the exposure is a quantity that is only defined for photons with energies below 3 MeV. Therefore, to determine the absorbed dose for any energy, the American Association of Physicists in Medicine (AAPM) introduced a protocol³² which is suitable for high energy beams and in any medium. Calibrations are based on a chamber specific calibration factor, N_{gas} , which can be calculated from N_x as follows:^{30,32}

$$N_{gas} = W_{air} \cdot N_x \left(2.58 \cdot 10^{-4} \frac{C}{kgR} \right) \left[\left(\frac{\mu_{abs}}{\rho} \right)_{air}^{wall} \left(\frac{L}{\rho} \right)_{wall}^{air} \right] \cdot A_{ion} \cdot A_{wall} \cdot \beta_{wall} \quad (2-5)$$

where W , N_x , and μ_{abs}/ρ are defined in equations (2-3) and (2-4). L/ρ is the restricted stopping power, in which only energy exchanges less than a set threshold energy are to be counted. A_{ion} , is the ionization collection efficiency at the time of calibration, A_{wall} , is a factor that corrects for attenuation and scatter in the wall of the chamber and build-up cap, and β_{wall} , is the quotient of absorbed dose by the collision fraction of kerma in the chamber wall. Note that the ratio of attenuation coefficients and stopping powers are to be evaluated for photon energies for which the exposure calibration, N_x , is available.

N_{gas} represents the calibration of the cavity gas in terms of absorbed dose to the gas in the chamber per unit charge or electrometer reading and it is a constant of the dosimeter as it is dependent on the volume and material of the chamber. Once N_{gas} is determined, the ionization chamber can be used to determine absorbed dose for a beam of any energy and in phantoms of any composition as follows³⁰

$$D_{med} = M \cdot N_{gas} \left[\left(\frac{\bar{L}}{\rho} \right)_{air}^{med} \right]^{hv} P_{ion} \cdot P_{repl} \cdot P_{wall} \quad (2-6)$$

Here M, is the charge collected by the meter, P_{ion} is the correction factor for the ionic recombination, P_{repl} is the factor that corrects for replacement of phantom material by an ionization chamber, and P_{wall} is the correction factor for the chamber wall and its surroundings, if they are of different compositions. The variables in brackets, in equation (2-6) are evaluated for the energy, $h\nu$ at which measurements are made.

II. Experimental Materials

2.4 The Medical Linear Accelerator (linac)

The linear accelerator (linac) shown schematically in Fig. 2.4 is a device that uses high frequency electromagnetic waves to accelerate charged particles such as electrons to high energies through an evacuated linear tube. The high energy electron beam itself after passing through scattering foils (Sec. 2.4.1) can be used for treating superficial tumors. Alternatively, electrons can also be used to strike high atomic number targets to produce x-rays for treating deep-seated tumors. A typical x-ray producing target (often referred to as the source) is tungsten, W, with an atomic number of $Z=74$.

Most modern radiotherapy linacs use power sources operating at 3000 MHz, giving them a wavelength in vacuum of:

$$\lambda = \frac{c}{\nu} = \frac{3 \times 10^{10} \text{ cm/s}}{3000 \times 10^6 / \text{s}} = 10 \text{ cm} \quad (2-7)$$

The time, T, for one oscillation of this power is $1/(3000 \times 10^6 \text{ s}^{-1}) = 333 \text{ ps}$. Medical linear accelerators can be of several types of designs, but the ones used in radiotherapy, accelerate electrons either by traveling or standing waves.^{3,29}

2.4.1 Major Components of a linac

The entire linac can be divided into two main parts; the stand, and the gantry as shown in Fig. 2.4. The stand which is anchored firmly to the floor of the treatment room houses major components such as;³

1. The Klystron, a microwave amplifier which is driven by a low-power microwave oscillator. It is essentially composed of two microwave cavities, a *buncher* cavity and a *catcher* cavity. Electrons emitted from the cathode by a negative pulse are directed towards the *buncher* cavity in which their velocity is altered by the action of an alternating electric field. As a result some electrons are speeded up while others are slowed down and some are unaffected. This results in bunching of electrons. As the electron bunches arrive at the *catcher* cavity which is resonant to the arrival frequency of the electron bunches, they generate an electric field which will decelerate the electrons, and by the principle of conservation of energy, the kinetic energy of the electrons is converted into high-power microwaves.

2. The waveguide. It conveys the power produced by the Klystron to the accelerator in the gantry.
3. The cooling water system. It is used for maintaining moderate temperature in various components that dissipate energy as heat.
4. The circulator. A device inserted in the waveguide to isolate the Klystron from microwaves reflected back from the accelerator.

The second part of the linac is the *Gantry*. It houses the following components;

1. The electron gun. It is triggered by a negative pulse from the power supply and electrons are injected into the accelerator structure as shown in Fig. 2.4.
2. The vacuum pump, provides the extremely low pressure needed for operation of the electron gun, the accelerator structure, and the bending magnet. Without a vacuum system the accelerated electrons would collide with air molecules, deflecting them and reducing their energy. The major components in the linac's *head* are illustrated in Fig. 2.5.
3. The bending magnet deflects the electrons emerging from the accelerator structure around a loop in order to strike the target to produce x-rays or to be used directly for electron treatments. Typically, a 270 degrees bending magnet is used in the design of medical linacs to bring the beam with energy spread to a single focal point on the target. This is done in part, by selecting the angle of the entrant and exit pole faces.³

4. The x-ray target, in a linac that has both an electron beam and x-ray beam mode, is retractable and is moved off axis for electron therapy. High atomic number materials are preferred as targets (typically Tungsten, $Z=74$) because of the probability and efficiency of bremsstrahlung production.
5. Primary collimators are placed next to the source to limit the maximum field size of x-rays produced in the target material.

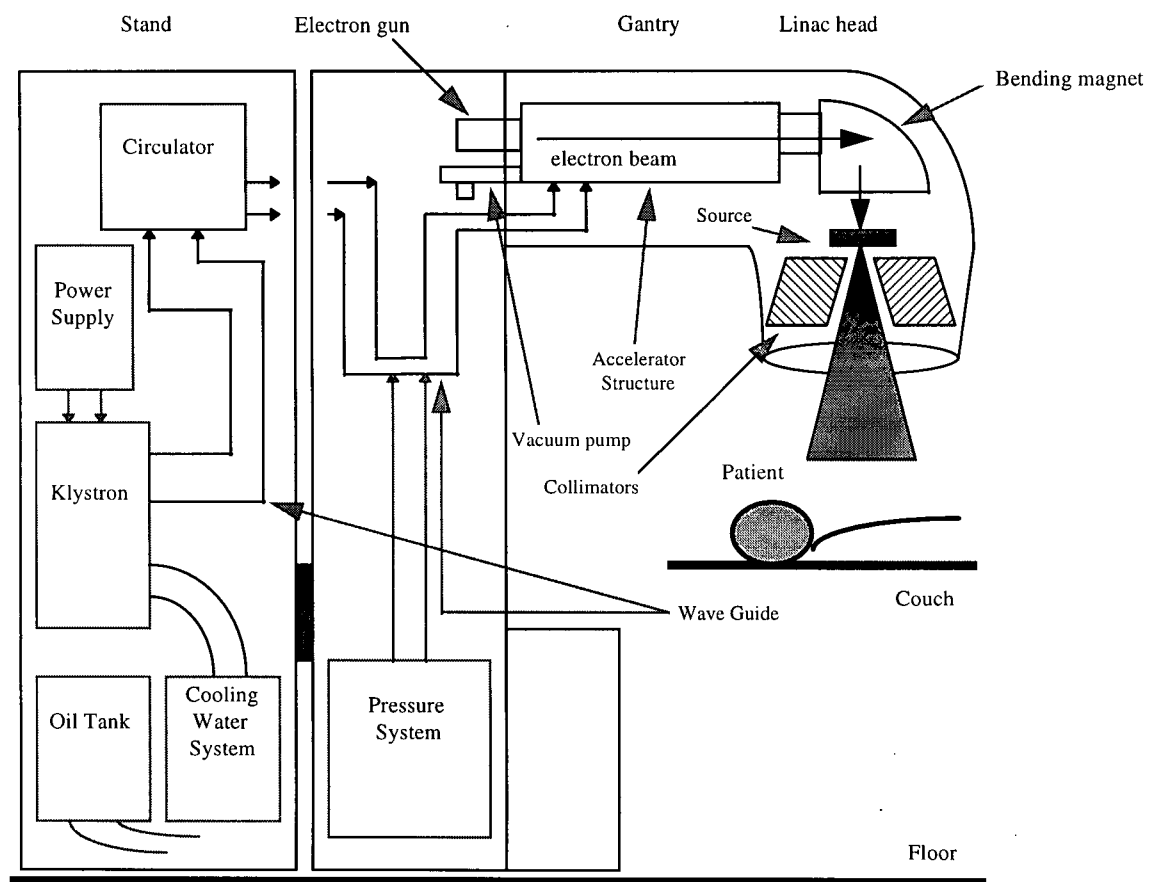


Figure 2.4: Schematic diagram of a high energy radiotherapy linac identifying major components housed in stand and gantry.

6. Flattening filter. Since linear accelerators produce electrons in the megavoltage range, the x-ray intensity is peaked in the forward direction as it exits the target material. To make the beam intensity uniform across the field, a flattening filter is inserted right after the primary collimators.

7. Scattering foil. In the electron mode of linac operation, the tungsten target is removed and the electron beam which emerges as a pencil beam from the bending magnet impinges on a scattering foil that has been moved in the place of the flattening filter using a carousel. The purpose of using a scattering foil is to spread the beam and obtain a uniform electron fluence across the treatment field. The material is usually made of one or more thin metallic foils of lead.

8. Monitoring chambers. To monitor the output radiation that is coming out of the linac head, three sets of ion chambers monitor the dose rate, integrated dose, and the field symmetry.

9. Secondary collimators. The beam is further collimated by two sets of movable jaws (secondary collimators) which can be used to produce various rectangular or square radiation field sizes. Newly designed *multileaf* collimators²³ (not shown here) are capable of producing irregular fields to fit the geometry of the treatment volume.

10. A range finder as well as radiation field light is also placed in the linac head to determine the distance from the surface of the skin to the source which is referred to as source to skin distance (SSD) and indicate the radiation field size.

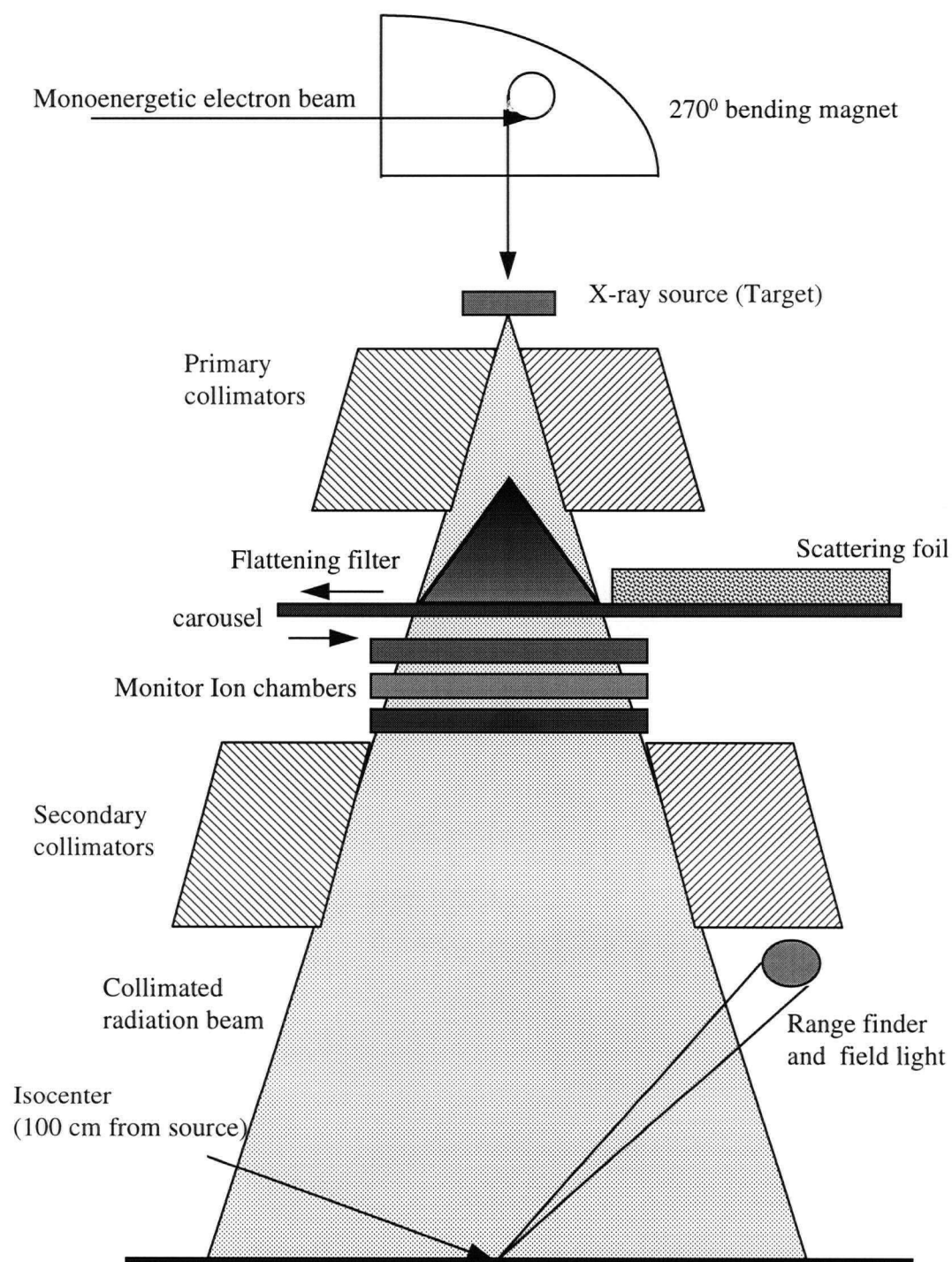


Figure 2.5: A schematic diagram of the linac treatment head with its major components is shown. The isocenter is typically the point 100 cm away from the source.

2.5 Linac Accessories

2.5.1 Wedge Filters

Perhaps the most commonly used beam modifying device in radiotherapy is the so called “wedge filters”. This is a wedge shaped absorber placed in the beam so that the spectral distribution of the radiation beam is changed [Fig. 2.6] and the isodoses are tilted. For use with high energy radiation, the wedge is usually made of dense material such as lead or steel.²⁹

The purpose of wedging a beam is that, there are particular clinical conditions that may not be treated adequately when using combinations of open beam fields.³¹ This is because the combinations of open fields may give rise to unacceptably large dose deposition across the tumor volume or surrounding tissues. However, combining two wedged beams can produce a uniform distribution of dose in the region of overlap of the beams.^{30,33,34} Figs. 2.6b-c illustrate the effect of wedge filters on radiation beams and the resultant dose distribution in a patient. Depending on the degree of change desired in dose distribution at a specified depth in a patient, the wedge can be made of varying slopes to provide the desired tilt in isodose curves (e.g., 15, 30, 45, and 60 degree slopes).

The presence of a wedge filter changes the output of the machine which must be accounted for in the calculation of absorbed dose in a patient. This effect can be characterized by the wedge factor, defined as the ratio of beam outputs with and without the wedge at a point along the central axis of the beam.²⁹ It can either be measured in air

or more typically in phantom at the depth of maximum dose. In air measurements require the appropriate build up cap for different energies.

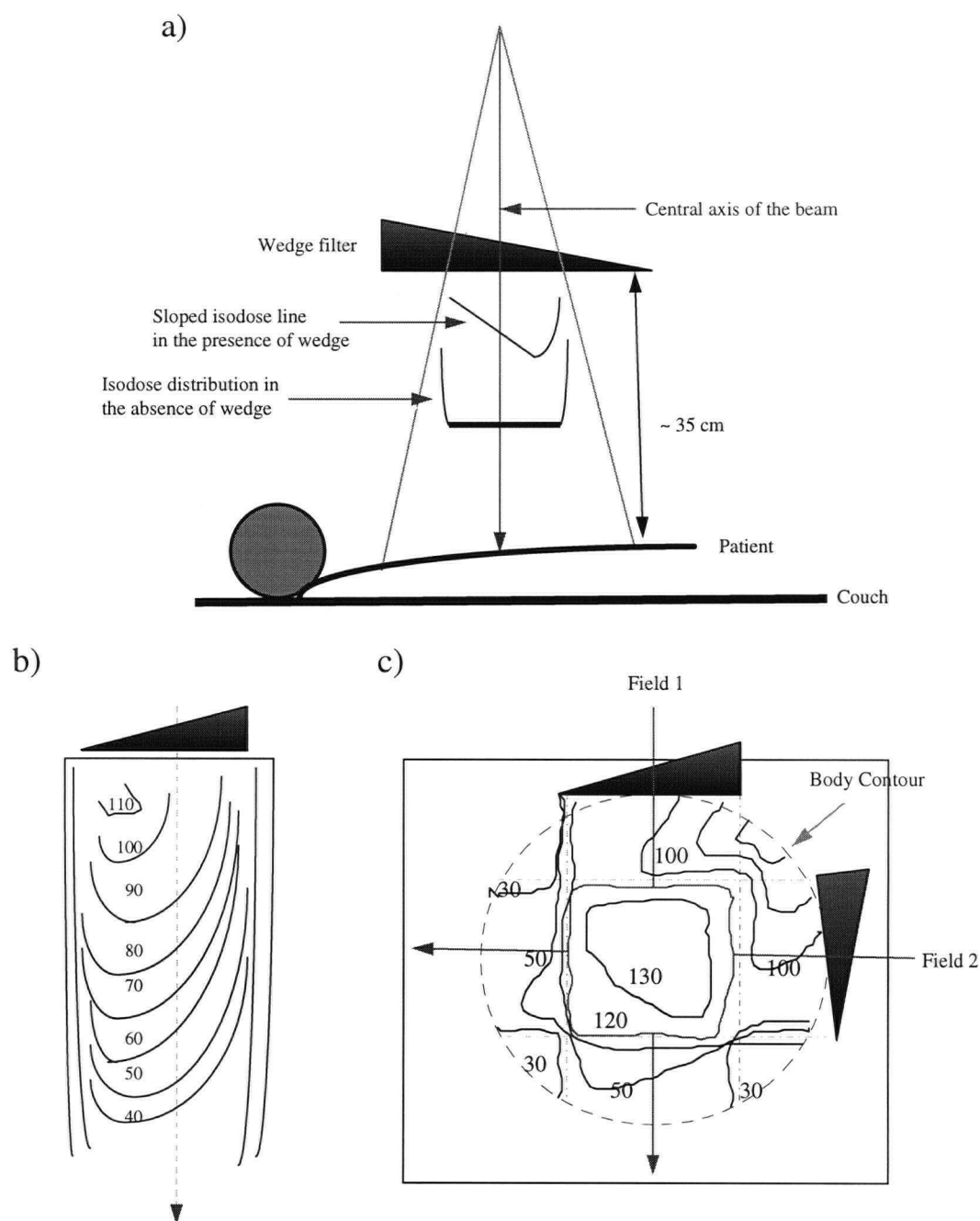


Figure 2.6: a) Schematic representation of a wedge filter. The distance between the skin surface of the patient and the wedge is made about 35 cm to preserve the dose build-up effect at the patient's skin surface. b) Dose distribution for a single beam incident on a flat phantom and c) dose distribution in a patient for a combination of wedged beams.

2.6 Radiation Dosimeters

2.6.1 Farmer-type Air Ionization Chamber

There are several ways by which a beam of radiation may be detected and a calibration or measurement of absorbed dose made. In addition to using the scanning liquid filled ion chamber portal imaging system which is described in detail in Chapter 1, one of the dosimeters used in measuring the absorbed dose in the present work is a 0.6 cm³ PTW Farmer-type air ionization chamber shown schematically in Fig. 2.7. The ionization chamber has a calibration factor traceable to a standards lab which is used in the calculation of absorbed dose according to equations 2.5 and 2.6.

The wall around the air cavity of this ionization chamber is shaped like a thimble. The material from which the wall is made, is matched in atomic number and photon absorption properties to the air in the cavity or to the material into which the chamber is inserted. The reason for this is to ensure that the energy spectrum of electrons liberated in the thimble wall is similar to that in air or medium (effective atomic number of air: 7.78).²⁹

The central electrode of the ion chamber, typically made of aluminum, is supplied with positive or negative charge by an external power supply. The inside surface of the wall is coated with a conducting material and may be grounded. Thus, a potential difference exists between the wall and the central electrode enabling the energetic electrons produced in the wall of the chamber to experience a force due to the electric field.³¹ The chamber is connected to an electrometer and the charge liberated in the chamber upon

irradiation is collected by the central electrode and then converted to absorbed dose by applying corrections for variations in temperature and pressure and other factors as discussed in Sec. 2.3.2.

It should be noted that in the measurement of absorbed dose, the concept of electronic equilibrium is important. It is achieved inside the cavity provided the wall thickness is equal to or greater than the maximum range of electrons in it to ensure that the electrons that cross the cavity arise in the wall and not in the medium. Therefore, a build-up cap may be necessary over the sensitive volume of the chamber so that the combined thickness of the chamber wall and the build-up cap is sufficient to provide charged particle equilibrium for a particular photon energy. The build-up cap is usually made of water equivalent material such as perspex (electron density relative to water 1.15) and must be in place when measuring radiation. Typically the required combined thickness of build-up cap and the wall of the chamber used for 6 MV photons is 1.5 cm and for 10 MV photons it is 2.5 cm.

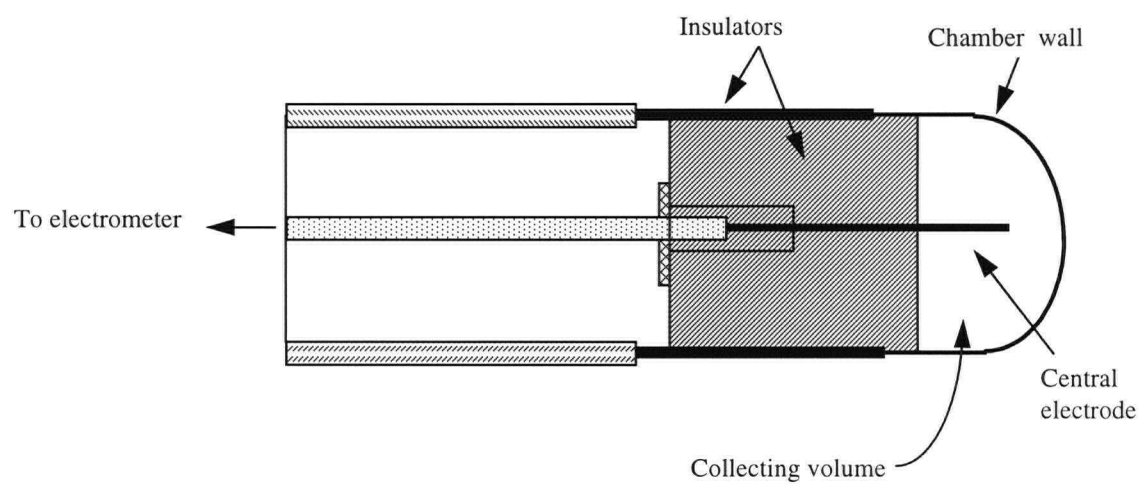


Figure 2.7: Schematic diagram of a Farmer-type ionization chamber (0.6 cm^3 PTW) is shown. The electrometer used in conjunction with the chamber was a Victoreen model 500.

2.6.2 Thermoluminescent Dosimetry (TLD)

Certain crystalline materials, when heated after irradiation, will emit light proportional to the amount of radiation to which they were exposed. The emission of light by the application of heat is called thermoluminescence. Thermoluminescent dosimetry (TLD) is a method for determining absorbed dose from thermoluminescence produced in appropriate crystals such as lithium fluoride, LiF. In these materials, impurities are contained in the crystal which in turn create imperfections in the form of energy traps [Fig. 2.8]. When the material is irradiated, some of the electrons in the valence band receive sufficient energy to be raised to the conduction band from where they migrate into the traps. The vacancy created in the valence band is thus called a positive hole which migrates into a hole trap. The number of electrons which are captured by the traps is proportional to the radiation dose to which the material has been exposed. At room temperature most of these electrons will remain trapped, however, if the material is subsequently exposed to a high temperature environment ($\sim 300^{\circ}\text{C}$), the kinetic energy of the molecules is increased and some of the electrons escape from the traps, recombine with holes and emit light photons. The emitted light is then collected by a photomultiplier tube (PMT) which converts the small amount of the emitted light into an electrical current so that it may be amplified and measured.

A plot of the thermoluminescence signal against temperature is called a glow curve. A glow curve may consist of a number of glow peaks corresponding to different energy

traps in the crystal. The area under the whole glow curve or peak heights can be related to absorbed dose.

An advantage of using TLDs for dosimetry purposes is their wide useful dose range (100 μGy to 10 Gy) and their small size configured in the form of rods, chips or powder makes them ideal to assess the radiation dose received by personnel or used in radiotherapy to measure the absorbed dose to critical organs such as the eye.

However, it should be noted that TLDs must be calibrated in a known radiation beam before they can be used. The response of the TLD material may be affected by their previous radiation and thermal history. The minimum sensitivity of TLDs (LiF) is about 100 μGy , and the signal remains linear with dose rate up to about 10 Gy. At higher doses, the material experiences a non-linear response per unit dose rate which is referred to as superlinearity.³⁵ In general an accuracy of $\pm 3\%$ can be achieved by TLDs.²⁹

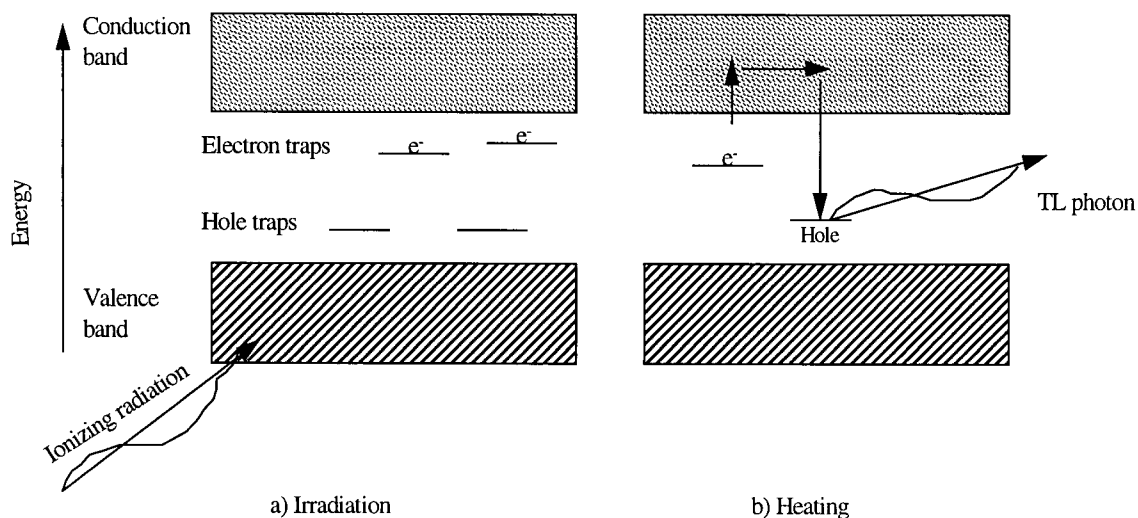


Figure 2.8: A simplified energy level diagram is shown to illustrate the thermoluminescence process in a crystal.

2.6.3 Semiconductor Detectors

The absorption of x-ray photons within semiconductor solid state detectors produces energetic electrons due to photoelectric and or Compton interactions. These then produce secondary electrons by ionization (electron-electron collisions). A potential difference across the semiconductor sweeps the electrons away from the site of their production, and results in a pulse of electricity whose magnitude is proportional to the number of electrons produced by irradiation and therefore the absorbed dose within the semiconductor. An advantage of using semiconductors, such as Silicon diodes, is that only 3.6 eV is required to produce an ion pair compared to 33.85 eV required by the air filled ion chamber. In addition the density of Silicon is 2.3 g/cm^3 which is about 18000 times that of air. Therefore, the sensitivity of the diode is approximately 1800 times that of an ion chamber of the same volume.³⁰

Solid state detectors do not have the same atomic number as that of soft tissue which make their absorption properties different. They are eventually damaged after high doses of radiation and need calibration in a known radiation beam.

2.7 Wellhofer (WP700) Water Tank System

The ion chamber and detectors such as Silicon diodes can be used in conjunction with a computer controlled water tank system for the measurement of dose at a given point or dose profiles across the radiation field. The system allows one to scan the

detector mechanically at various depths in water in different directions with respect to tank coordinates. The water tank is connected to a microcomputer and electrometer for analysis of beam output. In measurements performed using a Wellhofer water tank, a reference chamber is used in conjunction with the actual chamber in the tank. The function of the reference chamber is to correct for any fluctuations in output beam (dose rate). Because the dose rate may not be constant over a given number of monitor units (MUs), a reference chamber is used to measure the dose at a fixed point in air. The measured profiles are then the ratio of actual dose to the reference dose. This normalization of dose will correct for output variation of the machine across the field of view (FOV). Fig. 2.9 shows the major components of the Wellhofer (WP 700) water tank system.

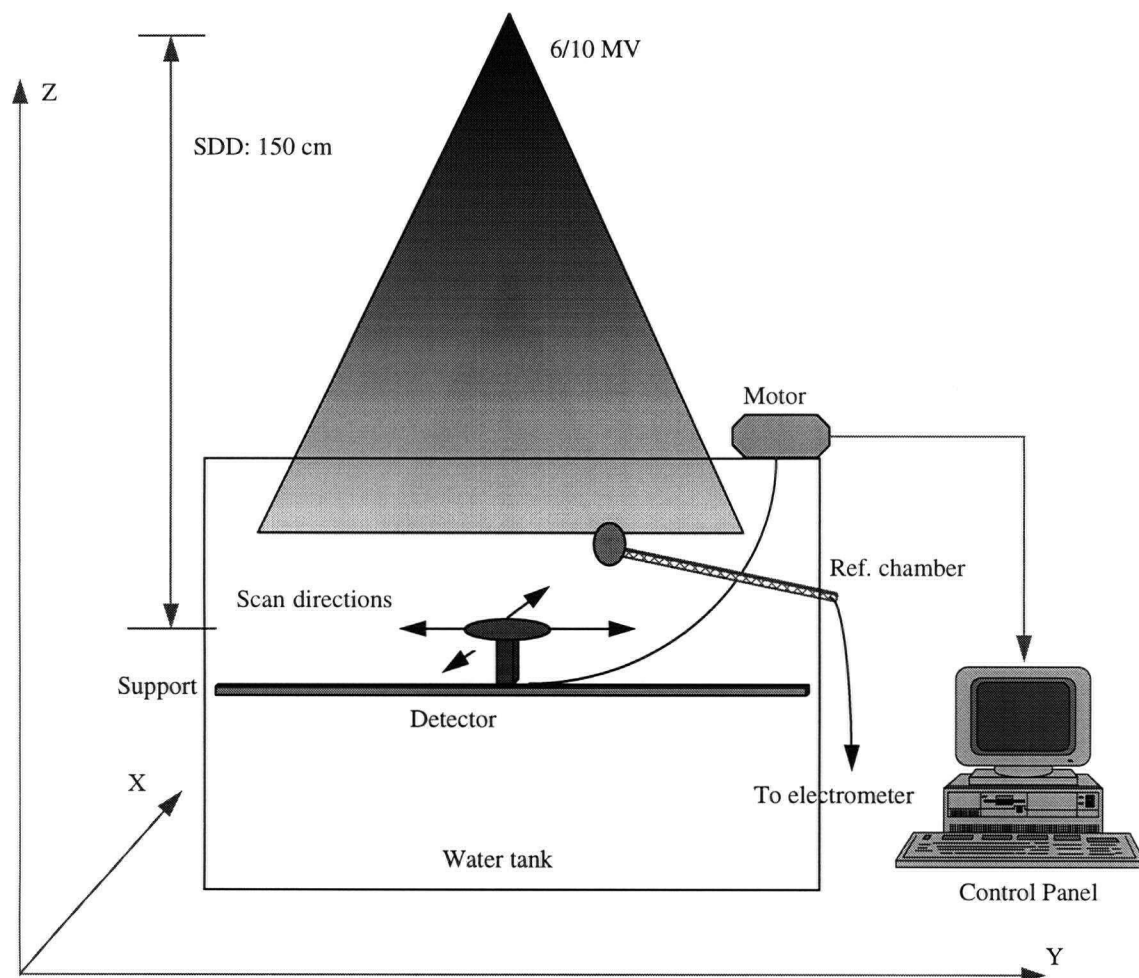


Figure 2.9: Cross sectional view of a water tank dosimetry system used for dose profile measurements, controlled by a Wellhofer (WP 700) dosimetry computer.

Chapter 3

Characteristic Curves of SLIC-EPID

3.1 Experimental Methods

Prior to the determination of the characteristic curves, the imaging system was calibrated according to the procedure described in Chapter 1. The calibration of the imaging device was performed for 6 and 10 MV photons and dose rates of 100, 200, and 300 monitor units per minute (MU/min). The acquisition mode for the Portal Vision™ system was set on standard sampling mode and the chamber cassette was positioned at a source to detector distance (SDD) of 150 cm. It is recommended for the commercial systems that the radiation field size covers only the sensitive area ($32.5 \times 32.5 \text{ cm}^2$) of the image detector to ensure that the electronic components housed in the vicinity of the detector are shielded and protected from being damaged by high energy radiation. For this reason, the calibration was performed with a radiation field size of $22 \times 22 \text{ cm}^2$ defined at 100 cm from the source.

The characteristic curves for three different radiation field sizes, 5×5 , 10×10 and $20 \times 20 \text{ cm}^2$, and two energies were obtained by relating the incident radiation intensity to the corresponding output pixel values. The incident radiation intensity was varied by

changing the source to detector distance (SDD) from 110 to 150 cm in steps of 10 cm. Moreover, the beam intensity was changed by varying the dose rate from 100 to 300 MU/min. The measure of the charge collected (pixel values) represents the average of 9x9 pixels taken at the central axis of the radiation beam and each data point on each graph is the average of three independent measurements taken on the same day and under the same conditions to test the reproducibility of the system. Fig. 3.1 illustrates the system set-up. Identical measurements are made with the ion chamber at the same position as the EPID.

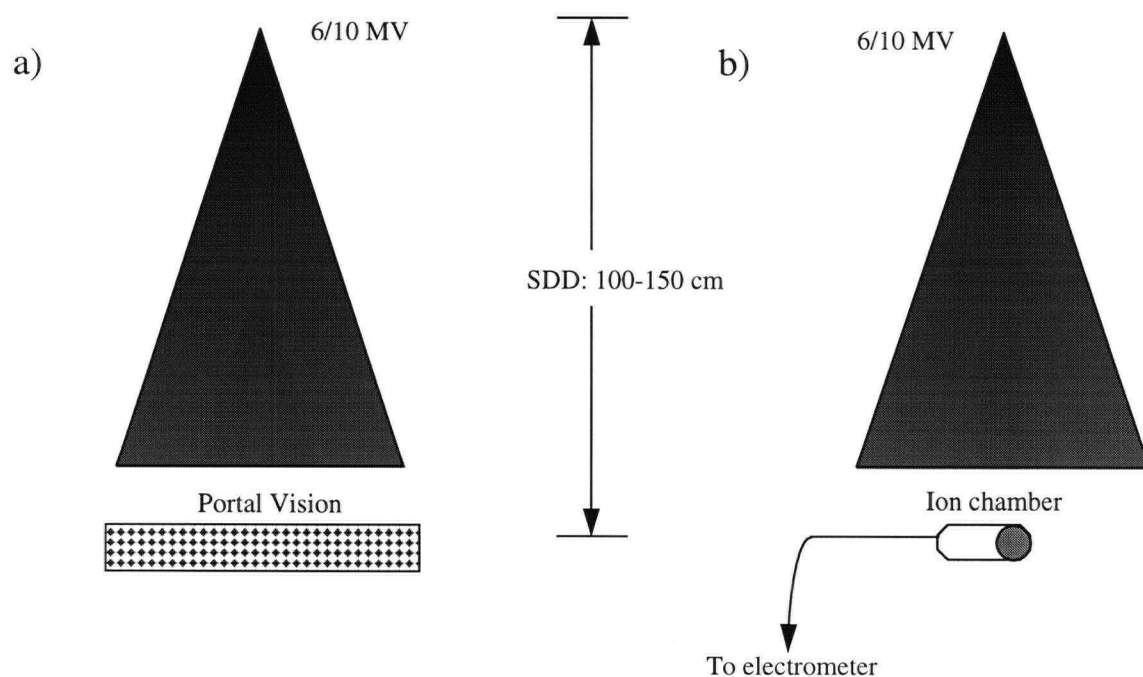


Figure 3.1: The schematic diagram of the system set-up for a) portal imager measurements and b) ion chamber measurements is shown.

3.2 Results

Figures 3.2-3.4 illustrate a set of characteristic curves obtained using the EPID at central axis of the beam for two photon energies and standard sampling mode. Each data point on the graphs represents the response of the imaging system to incident radiation intensity as a function of the ion chamber reading, M measured for the identical beam condition. The characteristic curves obtained for the 6 MV beam are comparable to those obtained with 10 MV photons. This implies that the response of the imaging device to the incident radiation intensity is comparable for different photon energies.²¹ Also according to van Herk's studies,²⁰ the collected charge (proportional to pixel value) should be proportional to the square root of the radiation intensity. This relationship was confirmed by plotting the data for various field sizes and energies and fitting to a simple square root model of the following form

$$PV = P_1 + P_2 [M]^{1/2} \quad (3-1)$$

where P_1 and P_2 are parameters determined by a best fit to the experimental data. PV is the average pixel value in a given region of interest (ROI) on the image and M is the corresponding reading of the electrometer. Rewriting equation (3-1) yields

$$M = \left[\frac{PV - P_1}{P_2} \right]^2 \quad (3-2)$$

where M can be used to calculate radiation absorbed dose delivered to a given ROI at the central axis according to equation (2-4).

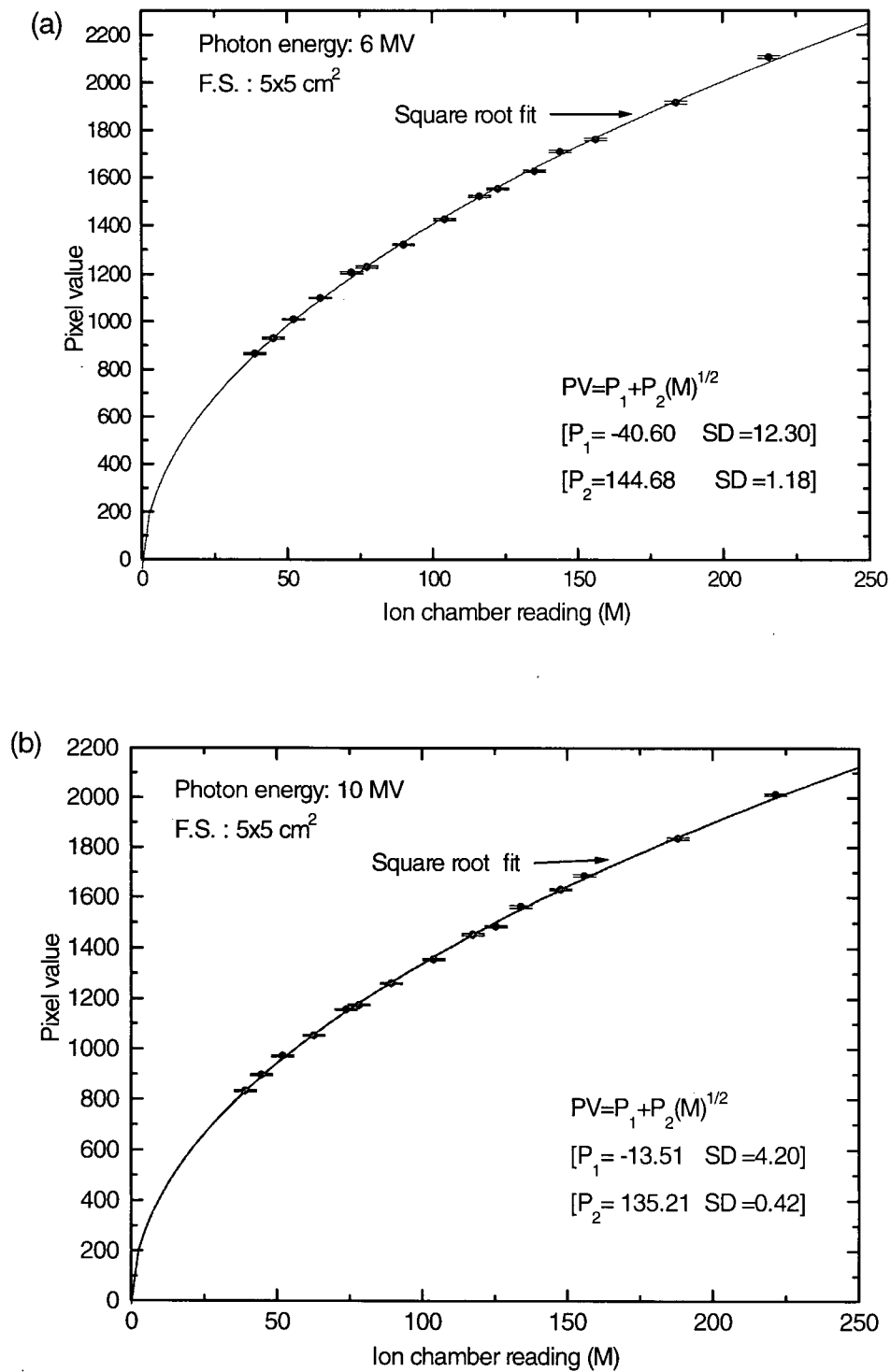


Figure 3.2: Characteristic curves are shown for a (a) 6 MV and (b) 10 MV beam for a 5x5 cm² radiation field size.

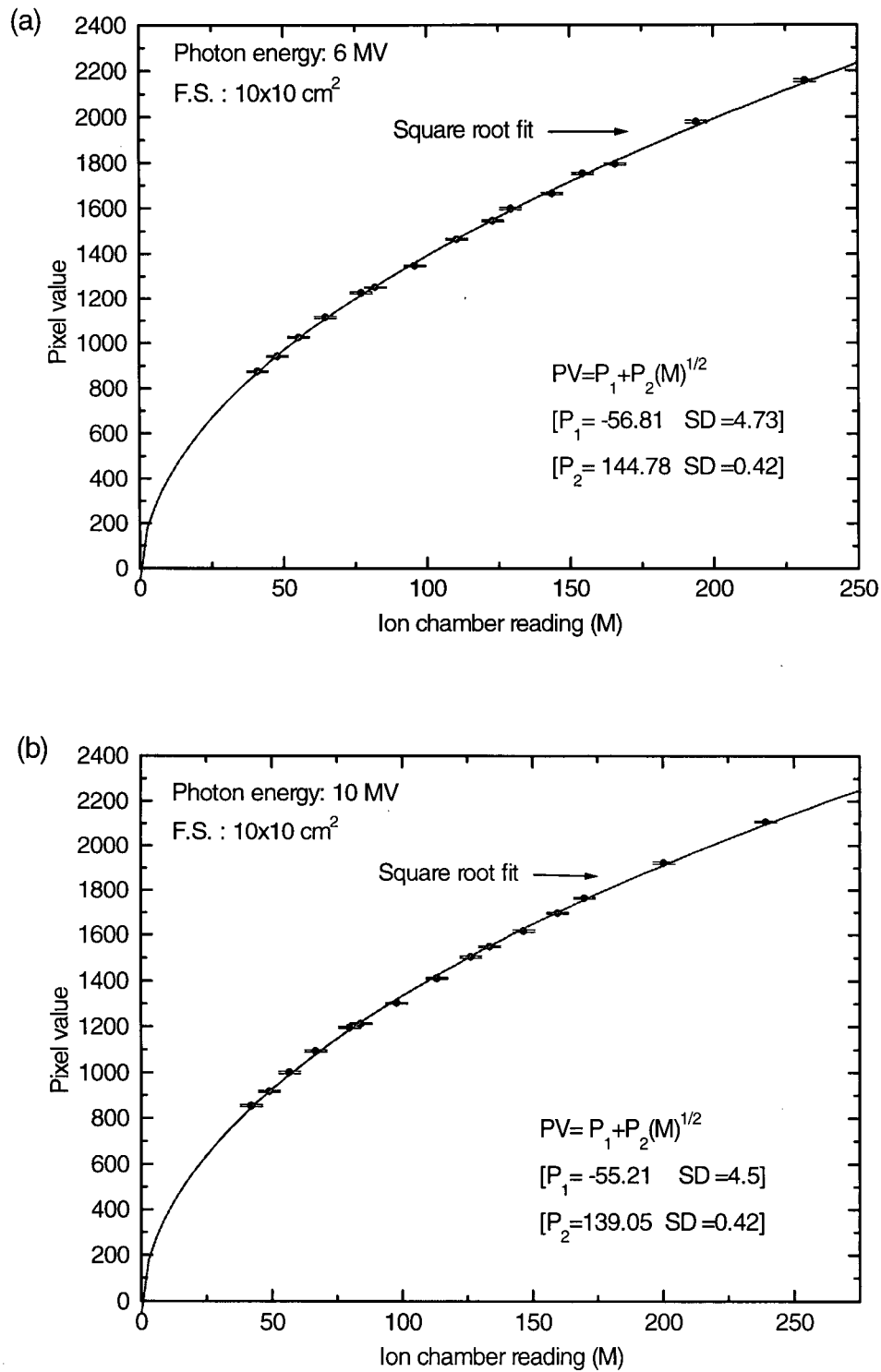


Figure 3.3: Characteristic curves are shown for a (a) 6 MV and (b) 10 MV beam for a 10x10 cm² radiation field size.

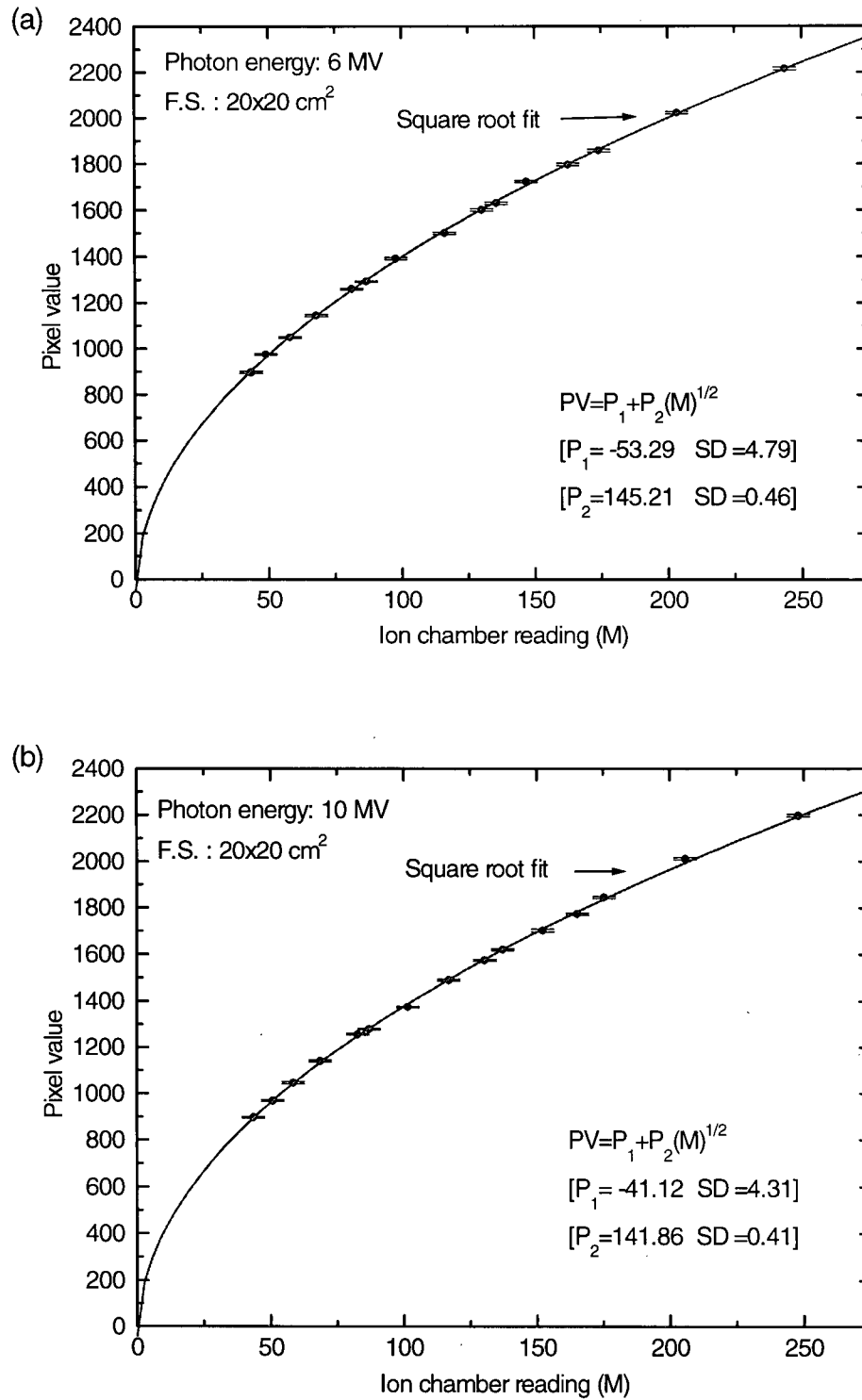


Figure 3.4: Characteristic curves are shown for a (a) 6 MV and (b) 10 MV beam for a 20x20 cm² radiation field size.

Figure 3.5 shows the data for all the field sizes plotted on a single graph. It can be seen from the results that the system performance experiences no field size dependence for the 6 MV beam, whereas, for the 10 MV photons, slight variation is seen as field size is increased from 5x5 to 20x20 cm². The maximum deviation between the fitted curve and the pixel values of the 20x20 cm² field size is 1.2% for the 10 MV beam.

The parameters, P_1 and P_2 and their associated standard deviations (SD) obtained for Fig. 3.5 were compared with the average values of P_1 and P_2 and their calculated average standard deviations from the individual characteristic curves in Figs. 3.2-3.4. A summary of parameters P_1 and P_2 associated with the square root function are shown in Table 3.2.1

Table 3.2.1: The parameters P_1 and P_2 of the square root model used to determine the dose response of the imaging device are listed with their standard deviations given in brackets

Photon energy	6 MV		10 MV	
Fitted parameters	P_1	P_2	P_1	P_2
Avg. values for all field sizes	-50.23 [7.2]	144.89 [0.68]	-36.61 [4.34]	138.70 [0.42]
Common fit to all field sizes	-50.5 [6.95]	144.93 [0.65]	-43.24 [14.4]	139.48 [1.34]

As it is shown above, the variations in P_1 and P_2 for both the common fit curve in Fig. 3.5 and the average values for all field sizes as shown in Figs. 3.2-4 are within the standard deviations shown in brackets. This suggests the possibility of using one set of parameters for various field sizes in the calculation of exit dose.

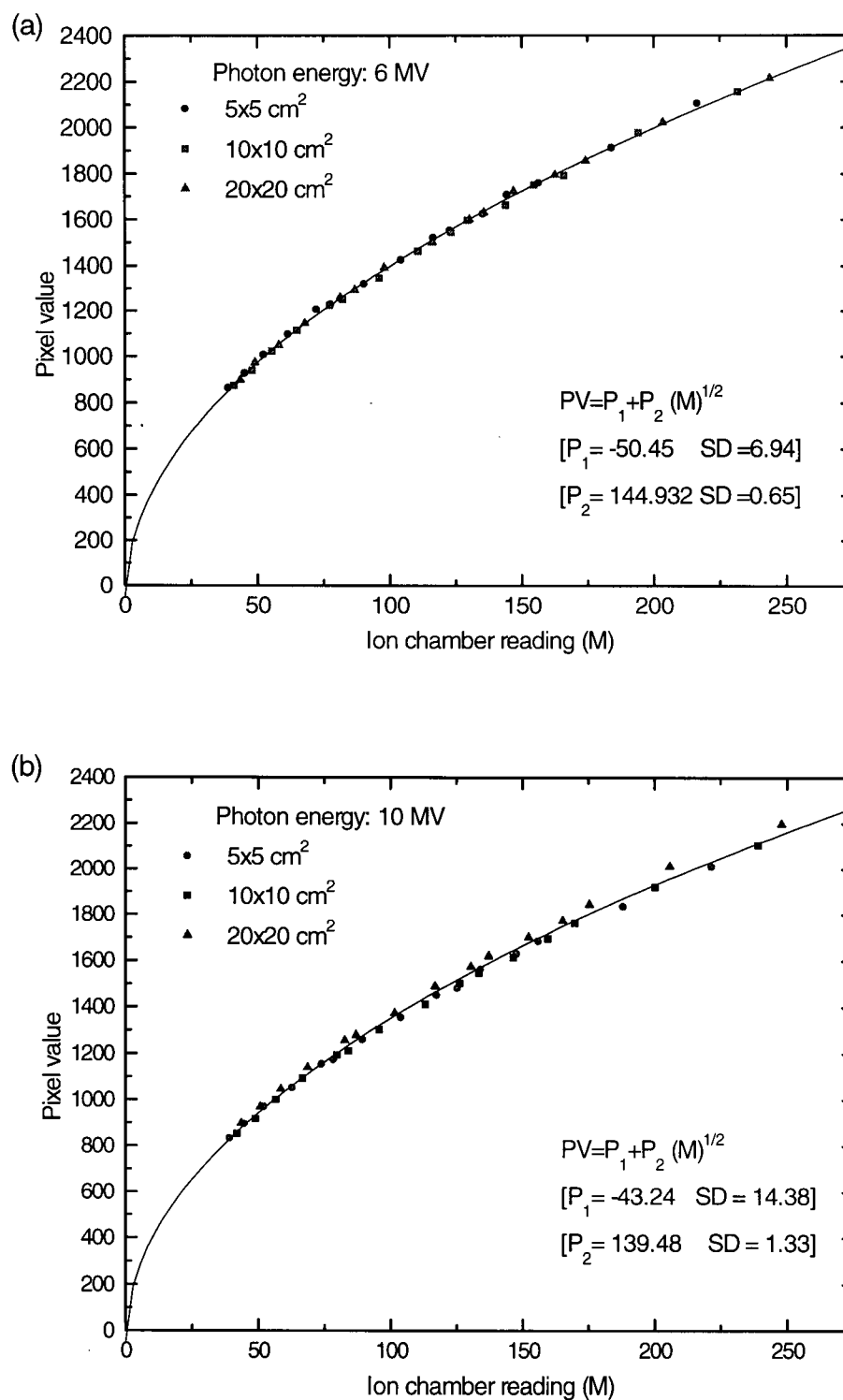


Figure 3.5: Superposition of characteristic curves for three field sizes is shown for (a) 6 MV and (b) 10 MV photons. The calculated parameters, P_1 and P_2 and their associated errors are obtained using a common fit for all the three field sizes.

3.3 Discussion

It is well known that the response of the SLIC is not a linear function of incident radiation intensity.¹⁹⁻²² The characteristic curves obtained in our measurements confirmed that the pixel values of the imaging device are dose dependent for both energies. This is because, as the ion chamber response, which is linearly proportional to the dose, increased, the pixel values of the imaging device show a non-linear response. However, for higher dose rates, the response of the system becomes more linear with beam intensity which is in agreement with the findings of other investigators.¹⁵

In Figures 3.2-3.4 the error bars represent the errors in average pixel values which are smaller than the data points and typically 5 to 6 pixel values. The error associated with the ion chamber readings is less than 1%.

The parameters, P_1 and P_2 are determined for the central axis of the beam (center of the detector). This will reduce the chances of fluctuations of the above parameters, since at off axis positions the radiation intensity generated by the accelerator is not exactly flat (due to horns) which will result in a variation in individual pixel sensitivity. Therefore, for practical reasons, it is convenient to determine the characteristic curves for the central region of the detector.³⁶

In Fig. 3.5-b it can be observed that for the 10 MV beam, as the field size increases to 20x20 cm², the pixel values deviate from the common fitted curve. This variation in system response with field size for the 10 MV beam could be due to the increasing scattered radiation which reaches the detector as the output energy of the machine is

increased. Although the characteristic curves seemed to have slightly different responses for larger field sizes for the 10 MV beam, it is safe to assume that the system's response is *nearly* independent of field size. This assumption may affect the dose calculation by at most 1% which is in an acceptable range.

Finally, the fact that the system is *nearly* independent of the field size, permits the use of one given field size for further dosimetric analysis of the detector.

Chapter 4

Transmission Dose Measurements

4.1 Experimental Methods

For the study of transmission (exit) dosimetry using the SLIC-EPID, various homogeneous phantom materials were used to simulate the attenuation of the beam which occurs clinically with the various body parts. For example, aluminum can be used to mimic the properties of bony structures in the body and perspex is used as muscle equivalent material.²⁹

A source to detector distance (SDD) of 150 cm with symmetric radiation field sizes of 5x5 and 10x10 cm² defined at isocenter were chosen for transmission dose measurements. A dose rate of 300 MU/min was used for both the 6 and 10 MV beams. The distance between the source and surface at which the beam enters the phantom material was varied by adding additional layers of phantom material of various thicknesses. However, the distance between the exit surface of the phantom material and the source was kept constant at 100 cm. The Portal Vision™ acquisition mode was set on standard sampling mode throughout these measurements and this in turn required approximately 30 MUs to acquire an image in six seconds. An ROI of 31x31 pixels at the central axis of the beam was selected for

averaging pixel intensities. Fig. 4.1 illustrates the geometry for the measurement of transmission dose.

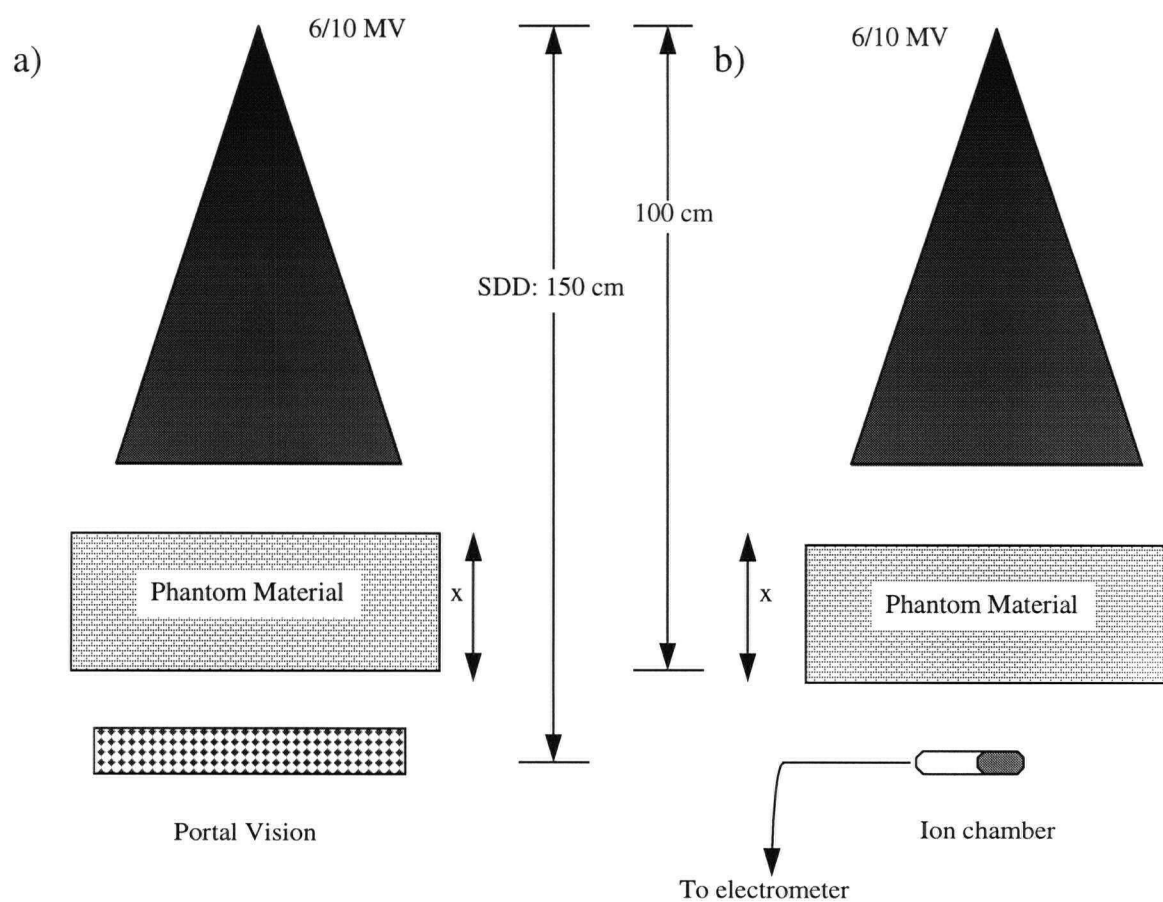


Figure 4.1: Schematic diagram of the geometry for relative exit dose measurements using a) the imaging system and b) ion chamber is shown.

To measure the actual exit dose for each phantom material, an ionization chamber was placed at the central axis of the beam, a distance of 150 cm from the source. A total of 100 MUs at a dose rate of 300 MU/min were used for all the ion chamber measurements. The dose to the detector was decreased by increasing the thickness of the attenuating material. The responses of the SLIC-EPID and the ion chamber for all the attenuating materials used were then normalized to the corresponding readings at zero thickness (open beam case) and compared to each other. The physical properties of the attenuating materials used are tabulated in Table 4.1.1.

Table 4.1.1: Physical properties of the phantom materials used.

<i>Constants</i>	<i>Perspex</i>	<i>Aluminum</i>	<i>Lead</i>
<i>Physical density g/cm³</i>	1.18	2.70	11.36
<i>Electron density Relative to water</i>	1.15	2.34	8.10
<i>Atomic number (Z)</i>	6.54	13	82
<i>Maximum thickness used (cm)</i>	22.5	4.5	1

4.2 Results

4.2.1 Perspex Phantom

Transmission (exit) dose measurements for both the calibrated ion chamber and the SLIC-EPID were obtained using perspex as attenuating material. The results for a 10x10

cm² field size are shown in Fig. 4.2. The response of the imaging system was analyzed by plotting normalized pixel values as a function of normalized ion chamber readings. One set of curves is obtained from uncorrected data, the other set is the data corrected for the non-linearity of the imaging system with the square root function and the parameters obtained using the characteristic curves as discussed in Chapter 3. Then, the exit dose at central axis of the beam may be calculated using the following relation and Equation (2-4):

$$M = \left(\frac{Avg. Pix. Val - P_1}{P_2} \right)^2 \quad (4-1)$$

where *Avg. Pix. Val* is the measure of average charge collected in a given ROI. The P_1 and P_2 used for the 6 MV beam are -50.45 and 144.93 respectively, and for the 10 MV beam -43.24 and 139.49 (Fig. 3.5, Chapter 3).

The transmission dose measured with the ion chamber is given by $(M/M_0)_{measured}$, where M_0 is the reading of the chamber without the attenuator, M is the reading after transmission through the attenuator. The corresponding averaged pixel values are $(PV/PV_0)_{measured}$. These, when plotted versus the measured (M/M_0) values, result in the upper dashed line shown in Fig. 4.2 (Uncorrected data) which demonstrate a non-linear relation. However, when the square root correction is applied as per Equation (4-1) and $(M/M_0)_{calculated}$ is plotted versus $(M/M_0)_{measured}$, a nearly straight line relation is obtained as shown in Fig. 4.2 (corrected data). $(M/M_0)_{calculated}$ from Equation (4-1) equals $(M/M_0)_{measured}$ and is given by

$$\left(\frac{M}{M_0} \right)_{calculated} = \left(\frac{PV - P_1}{PV_0 - P_1} \right)^2 \quad (4-2)$$

The straight line going through the origin in Fig. 4.2 indicates the ideal response, if the system were linearly dependent on dose. The maximum deviations between the SLIC-EPID response and that of the ion chamber with perspex as attenuating material for different field sizes and energies are given in Table 4.2.1.1. The maximum percentage deviation in dose ratio measured by the SLIC-EPID and that of the calibrated ionization chamber is 2% for both nominal energies after correction.

Table 4.2.1.1: Maximum deviations between attenuation measurements through perspex obtained with the EPID as compared to those obtained with a calibrated ion chamber are shown before and after correction for non linearity of system response.

<i>Attenuating material</i>	<i>Perspex</i>			
<i>Field size</i>	<i>5x5 cm²</i>		<i>10x10 cm²</i>	
<i>Photon energy</i>	<i>6 MV</i>	<i>10 MV</i>	<i>6 MV</i>	<i>10 MV</i>
<i>Max. deviation before correction</i>	42.0%	33.0%	40.0%	33.0%
<i>Max. deviation after correction</i>	1.0%	1.0%	2.0%	2.0%

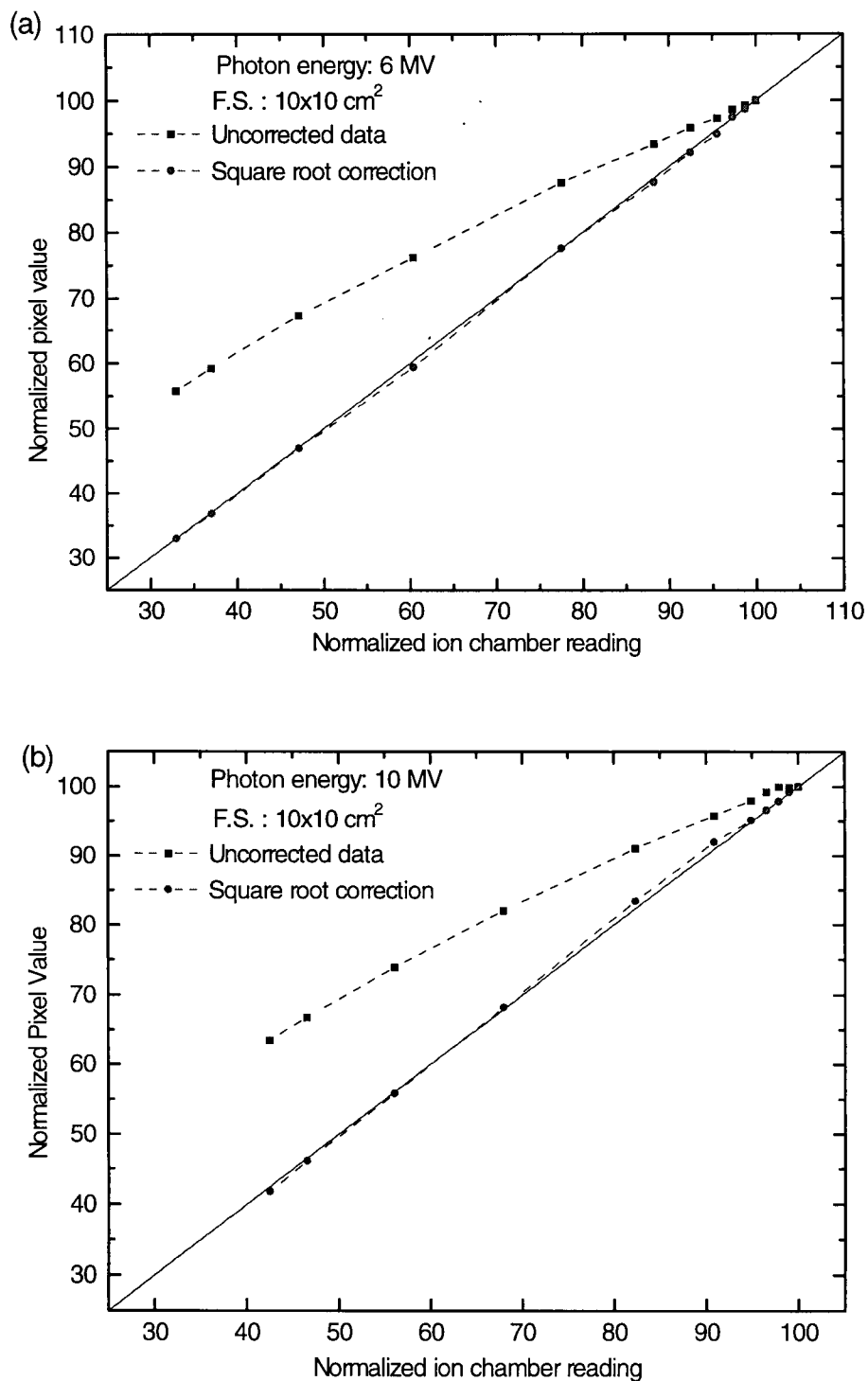


Figure 4.2: Normalized pixel values obtained by SLIC-EPID from transmission measurements through perspex are compared to normalized ion chamber readings before and after correction for system non-linearity for (a) 6 MV and (b) 10 MV photons.

4.2.2 Aluminum Phantom

Measurements were repeated with aluminum phantoms for field sizes 5x5 and 10x10 cm² at the central axis of the radiation beam. In Fig. 4.3 is illustrated the comparison of the SLIC-EPID response to the calibrated ion chamber. As before, data for both the Portal Vision™ and the ion chamber are normalized to the zero thickness readings. Table 4.2.2.1 is a summary of the Aluminum measurements for various field sizes and energies before and after the system's non-linear response is corrected. The maximum deviation after correction is 3%.

Table 4.2.2.1: Maximum deviations between attenuation measurements through aluminum obtained with the EPID as compared to those obtained with a calibrated ion chamber are shown before and after correction for non linearity of system response.

<i>Attenuating material</i>	<i>Aluminum</i>			
<i>Field size</i>	<i>5x5 cm²</i>		<i>10x10 cm²</i>	
<i>Photon energy</i>	<i>6 MV</i>	<i>10 MV</i>	<i>6 MV</i>	<i>10 MV</i>
<i>Max. deviation before correction</i>	21.0%	17.0%	20.0%	17.0%
<i>Max. deviation after correction</i>	3.0%	3.0%	2.0%	2.0%

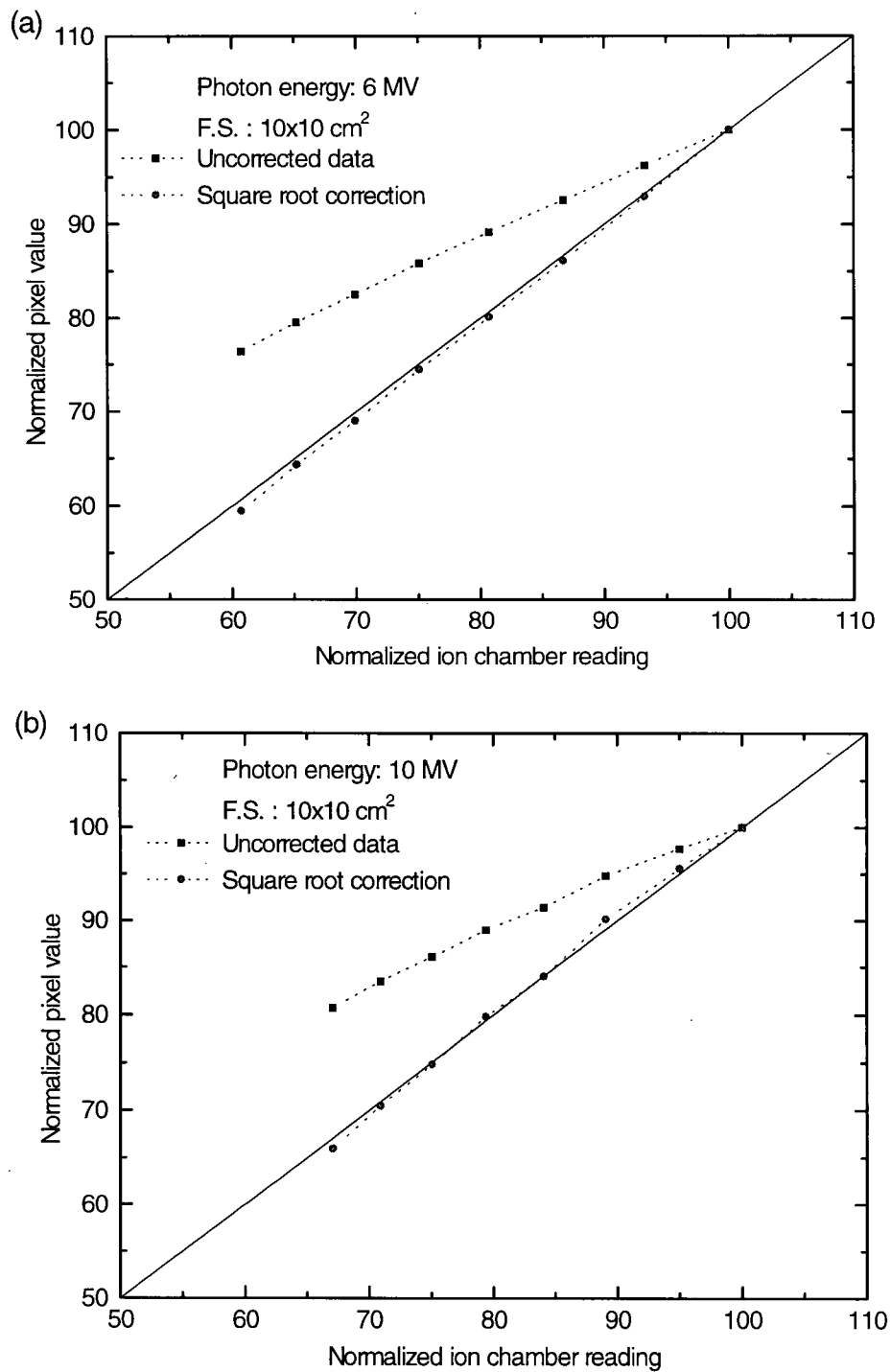


Figure 4.3: Normalized pixel values obtained by SLIC-EPID from transmission measurements through aluminum are compared to normalized ion chamber readings before and after correction for system non-linearity for (a) 6 MV and (b) 10 MV photons.

4.2.3 Lead Phantom

The results for transmission dose measurements through lead as phantom material for two field sizes, 5x5 and 10x10 cm² are shown in Fig. 4.4. Data for both the ion chamber and the Portal Vision™ are normalized to zero thickness readings. A summary of the percentage deviations observed between the SLIC-EPID and the ion chamber data at central axis is shown in Table 4.2.3.1. The maximum deviation after correction is 2.1%.

Table 4.2.3.1: Maximum deviations between attenuation measurements through lead obtained with the EPID as compared to those obtained with a calibrated ion chamber are shown before and after correction for non linearity of system response.

<i>Attenuating material</i>	<i>Lead</i>			
<i>Field size</i>	<i>5x5 cm²</i>		<i>10x10 cm²</i>	
<i>Photon energy</i>	<i>6 MV</i>	<i>10 MV</i>	<i>6 MV</i>	<i>10 MV</i>
<i>Max. deviation before correction</i>	25.0%	22.03%	23.9%	22.2%
<i>Max. deviation after correction</i>	1.0 %	2.1%	1.0%	1.8%

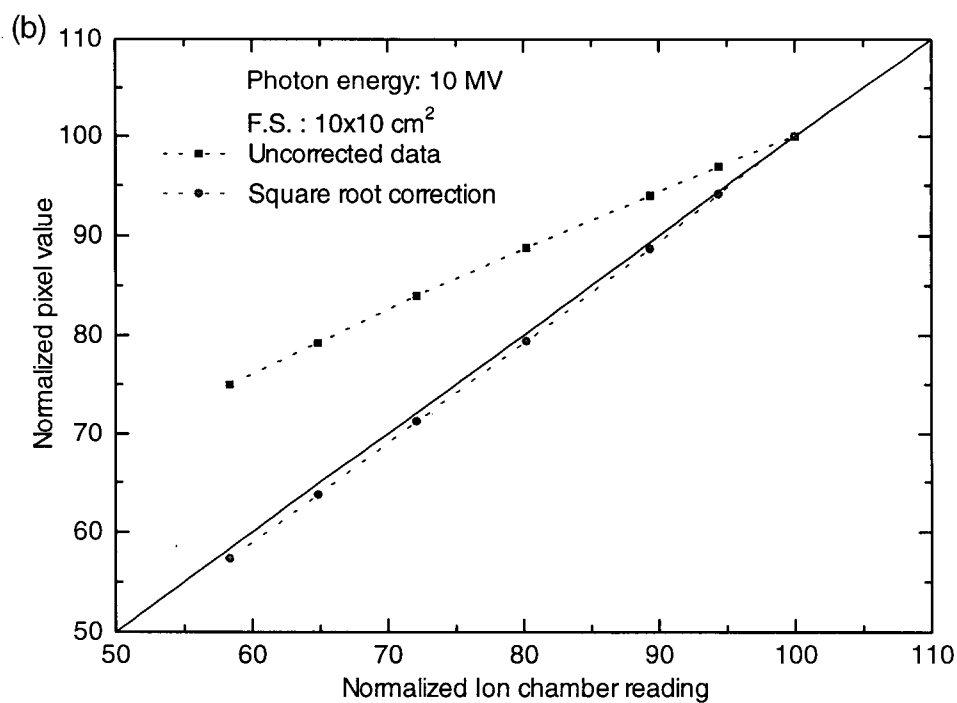
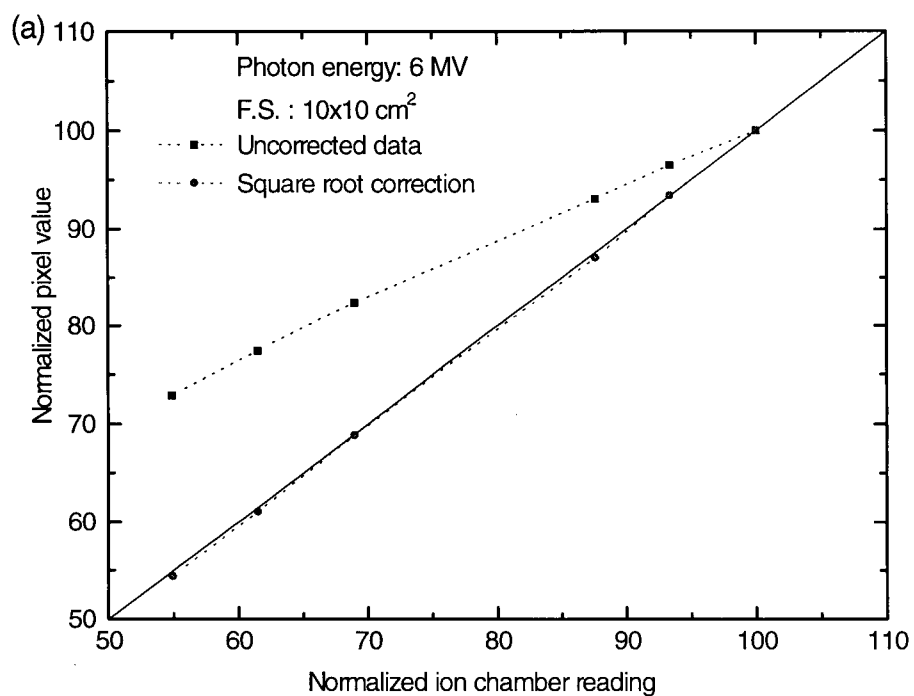


Figure 4.4: Normalized pixel values obtained by SLIC-EPID from transmission measurements through lead are compared to normalized ion chamber readings before and after correction for system non-linearity for (a) 6 MV and (b) 10 MV photons.

4.3 Discussion

The reproducibility and accuracy of a commercial matrix of ion chambers as an alternative to already recognized *in-vivo* dosimetry methods such as TLDs and diodes for dose verification during treatment was investigated.^{10,27,28}

The response of the system was studied by comparing it to the response of a calibrated ionization chamber as the intensity of the output beam was changed by placing various homogeneous attenuating material of different densities and effective atomic numbers in the path of the beam. This is analogous to the clinical situation in which variation in beam intensity at the exit surface of the patient may be measured to obtain information about the dose distribution in the patient and compare it with planned dose calculations.

The maximum deviation of the SLIC-EPID response from that of the ion chamber for two photon energies used was less than 3% after correction for the non-linearity of the system.

Possible sources of error that may have contributed to this discrepancy are:

1. Measurements of both detectors were not taken simultaneously to avoid any variation in beam output.
2. The EPID has been constructed from different materials than the ionization chamber and a different energy dependence of EPID response is therefore expected.
3. More importantly, other factors such as inadequate buildup material on the portal imager detector, lack of back scatter material for the ionization chamber and various

scattering conditions for each dosimeter may have an effect on the difference in response of the two detecting devices.

In summary, however, it should be stressed that these type of EPIDs are parameter dependent (Chapter 3) and a given set of parameters needs to be determined specifically for the type of imaging device used in the calculation of exit dose, as they may have different sensitivities to accelerator settings such as radiation dose rate, gantry angle, sampling mode, and energy.^{15,36} However, once the correct parameters are determined to account for the non-linearity of the pixel values measured by the SLIC-EPID, it is found to give a measure of relative exit dose on the central axis of the beam to within 3% accuracy.

Chapter 5

Portal Dose Profiles

5.1 Introduction

The commercial SLIC-EPID, when used for on-line geometrical verifications of anatomical structures, for a given energy and dose rate, automatically corrects for large variations in the sensitivity of individual pixel values across the detector area.^{11,37} Consequently, the output of the individual chambers are adjusted according to the radiation intensity impinging on the detector. Without this correction, the portal imager has limited clinical value for imaging purposes.¹⁹ The correction matrix required to correct this sensitivity variation in pixel values can be obtained by irradiating the imaging system with a radiation beam which is flat across the field of view (FOV). In practice, however, flat radiation beam profiles are difficult to obtain and therefore, this is performed with a beam whose intensity varies across the radiation field. This variation in beam intensity is mainly due to the fact that more energetic photons produced by the impinging electrons on the target material are peaked forward along the central axis of the beam which will cause a pronounced variation in beam intensity across the FOV. Although calibration of the portal imager in a non-

uniform field is adequate for imaging purposes, it limits the accuracy with which one can obtain dosimetric information. Therefore, to minimize the error inherited by the calibration of the system, one must use the most uniform radiation field that can be achieved.

The introduction of a flattening filter in the radiation beam, in the linac, is intended to produce a flat radiation field at a given depth in water.²⁹ Therefore, to determine the optimal depth in water at which a flat profile is achieved, a series of ion chamber scans in a water phantom (Chapter 2) were obtained. These cross-plane dose profiles are shown in Fig. 5.1 for a source to detector distance (SDD) of 150 cm where the field size was 60.3x60.3 cm². The water level above the chamber was varied from 2 cm to 11 cm in steps of 1 cm. The ion chamber scans at all depths in water were first smoothed and then normalized to central axis dose.

The field flatness of the ion chamber dose profiles, defined³⁰ as the variation of dose relative to the central axis dose over the given field size is calculated by

$$F = \left(\left| \frac{D_{CAX} - D_{max}}{D_{CAX}} \right| \right) 100 \quad (5-1)$$

where D_{CAX} is the dose at central axis of the beam and D_{max} is the dose maximum in the given field size. At 11 cm depth in water the field flatness is 1.6% for the 6 MV beam and 1.3% for the 10 MV photons as shown in Table 5.1.1.

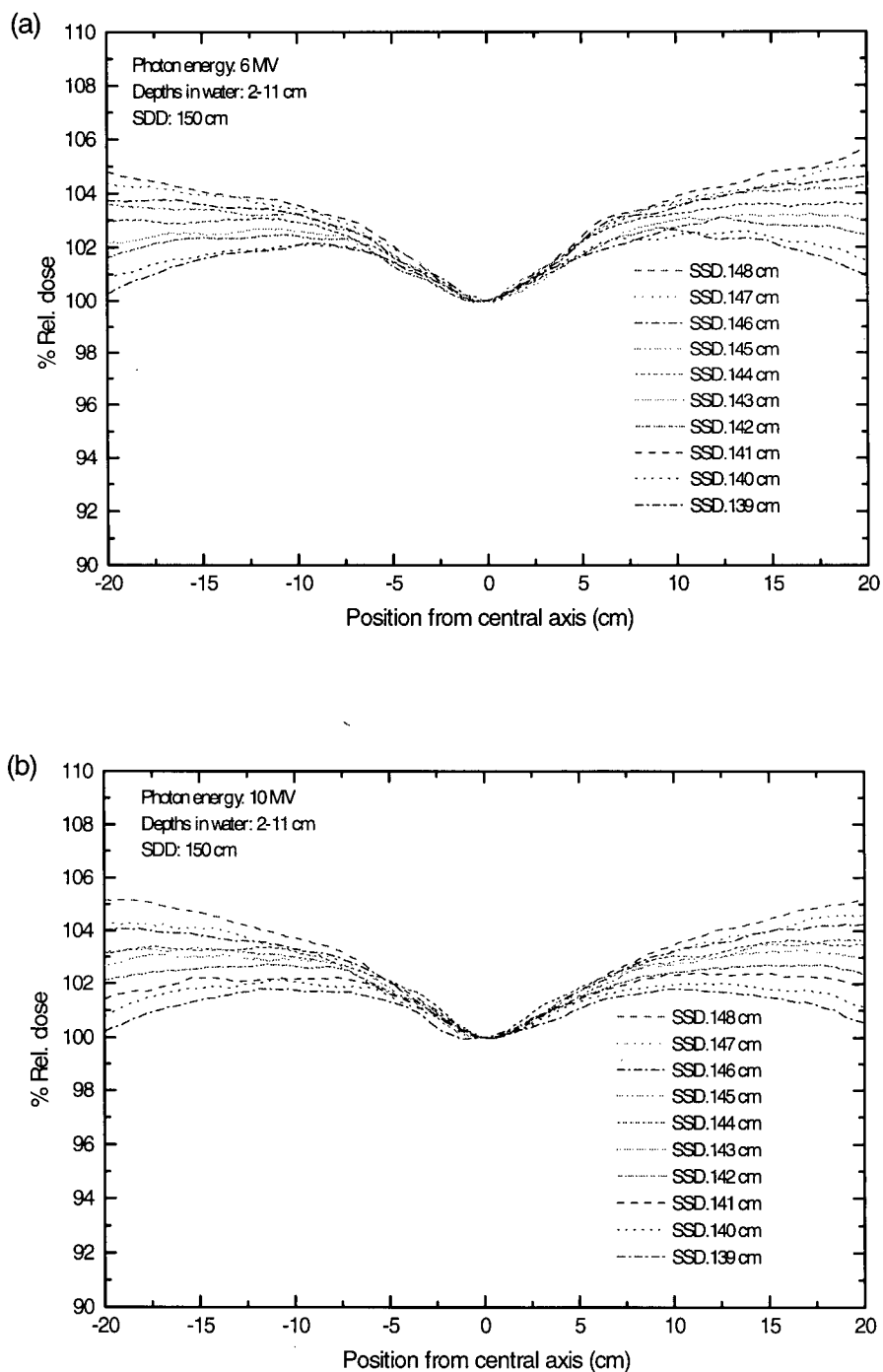


Figure 5.1: The cross-plane dose profiles measured with an ion chamber at various depths in water for (a) 6 MV and (b) 10 MV beams are shown. The source to detector distance (SDD) was kept constant while the water level above the detector was raised resulting in different source to surface distances (SSDs).

From these profiles, it is apparent that at shallow depths a large variation exists in response of the portal imager on central axis of the beam in comparison to the field edges. Table 5.1.1, shows the tabulated variations for different depths between central axis and a point 15 cm away from beam axis. It should be noted that increasing the depth beyond 11 cm produces only minimum improvement in field flatness.

Table 5.1.1: The variation in dose measured between the field edges (at 15 cm off axis distance) and the central axis for various depths in water and a field size of 60.3x60.3 cm² at the 150 cm distance from the source.

<i>Depth in water (cm)</i>	<i>6 MV</i>	<i>10 MV</i>
<i>1 cm (SSD:149 cm)</i>	6.0%	7.0%
<i>2 cm (SSD:148 cm)</i>	5.0%	5.0%
<i>5 cm (SSD:145 cm)</i>	4.0%	3.4%
<i>11 cm (SSD: 139 cm)</i>	1.6%	1.3%

From the above table, it is seen that the best possible flat field may be attained by placing 10 cm of perspex (electron density relative to water, 1.15) as water equivalent material on top of the matrix of ion chambers.

All data obtained with the imaging system (Portal Vision™) and presented in this Chapter are corrected for the system's non-linear response according to the procedure described in Chapter 4. Also, in this Chapter, the system is referred to be in *imaging mode* (IM) if no build-up material is used in the calibration of the system, and when additional material is placed on top of the detector for calibration, it is referred to be in *dosimetric mode* (DM).

5.2 Experimental Methods

5.2.1 Calibration of SLIC with Build-up Material

The procedures followed prior to the measurements of dose profiles in dosimetric mode were as follows;

1. Water equivalent material (perspex) of a thickness (10 cm) equal to that determined from the ion chamber measurements to give flat profiles was used to cover the matrix of scanning liquid-filled ion chambers. Therefore, a block of perspex with dimensions of $32 \times 32 \times 10 \text{ cm}^3$ was used for this procedure.
2. The cover of the imaging system which is used to protect the electronic components, housed in the vicinity of the matrix of ion chambers from crashing with couch or other objects was removed. This permits the phantom material to be positioned directly above (0.5 mm) the chamber matrix. The weight of the phantom was supported by two hydraulic jacks as shown in Fig. 5.2.
3. The imaging device was then calibrated according to the procedure described in Chapter 1 with the perspex block on top of the detector. Once the calibration was performed, the phantom material was removed and no longer used for subsequent measurements. This is different from the procedure described by Boellaard *et al*³⁶ which requires constant positioning of the build-up material on top of the imaging system. The protective casing of the detector was then placed back in its position so that the physical configuration of the detector remained similar to that used in clinical situations. The

system calibration in this manner represents the dosimetric mode (DM) of the imaging device.

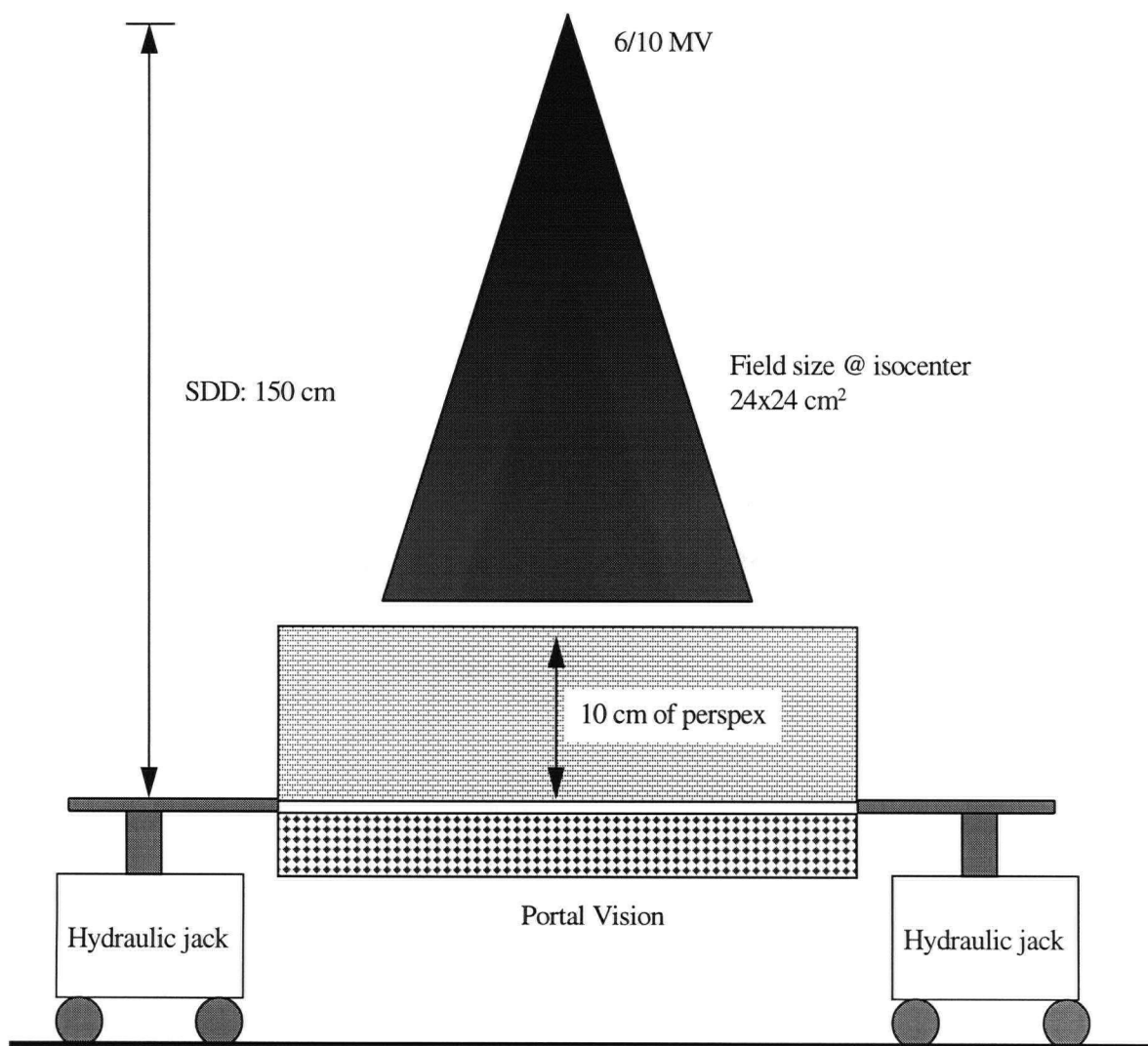


Figure 5.2: Cross section of system set-up for the calibration of portal imager for dosimetric mode. The cassette of the portal imager is covered with a block of water equivalent material and the field size is collimated to cover the sensitive area of the portal imager at the 150 cm distance from the source.

5.2.2 Wedged Dose Profiles

After calibrating the detector of the SLIC in dosimetric mode, the imaging system was positioned at 150 cm SDD and was irradiated with open fields and with clinically used wedge filters of various angles (15° , 30° , 45° , and 60°) in the beam. Wedges were placed in the beam a distance of 57 cm from the source. Dose profiles for both the open field and in the wedge direction were measured for both the 6 and 10 MV photons, with field sizes collimated to 5×5 , 10×10 and 15×15 cm² at isocenter and a dose rate of 300 MU/min. Dose profile measurements were carried out in both the imaging mode and the dosimetric mode of the SLIC. The individual dose profiles in both modes of the SLIC were first corrected for their square root dependence and then normalized to the corresponding open field profile.

Identical measurements were performed using an ionization chamber scanned with the Wellhofer™ dosimetry system (Chapter 2) and appropriate buildup caps in air. Wedged dose profiles were then similarly normalized to their corresponding open field dose profile. This was achieved by measuring the wedge factors, defined in Chapter 2, for different field sizes and energies at a source to detector distance (SDD) of 150 cm. The profiles were then normalized on central axis using the wedge factors.

5.3 Results

Open field and wedged dose profiles obtained with the imaging device were compared to those measured with the ion chamber for various field sizes. Figures 5.3a and 5.4a show the profiles measured with the SLIC in imaging mode compared to ion chamber profiles and Figs. 5.3b and 5.4b show the comparison of ion chamber profiles and the SLIC in dosimetric mode for a $15 \times 15 \text{ cm}^2$ field size.

In dosimetric mode [Figs 5.3b, 5.4b], the portal dose profiles (open field and wedged profiles) show a good agreement with that of ion chamber measurements in general. However, in imaging mode [Figs. 5.3a, 5.4a], the comparison between the two detector dose profiles reveals a pronounced discrepancy at the beam edges. The maximum deviation on the central axis of the beam between the ion chamber and the SLIC in dosimetric mode was calculated to be as high as 3.5%.

It should be noted that the center of the portal imager detector is not exactly aligned with the beam axis, therefore, for the purpose of dose profile comparison to that of ion chamber measurements which was positioned on central axis, the x-axis of dose profiles had to be re-scaled at 50% dose to correct for this problem. This was done by taking the ratio of the ion chamber reading at 50% dose to portal imager reading at the same point. It should also be noted that in portal imager dose profiles each point in the graphs is the average of 5×1 pixels resulting in a good spatial resolution.

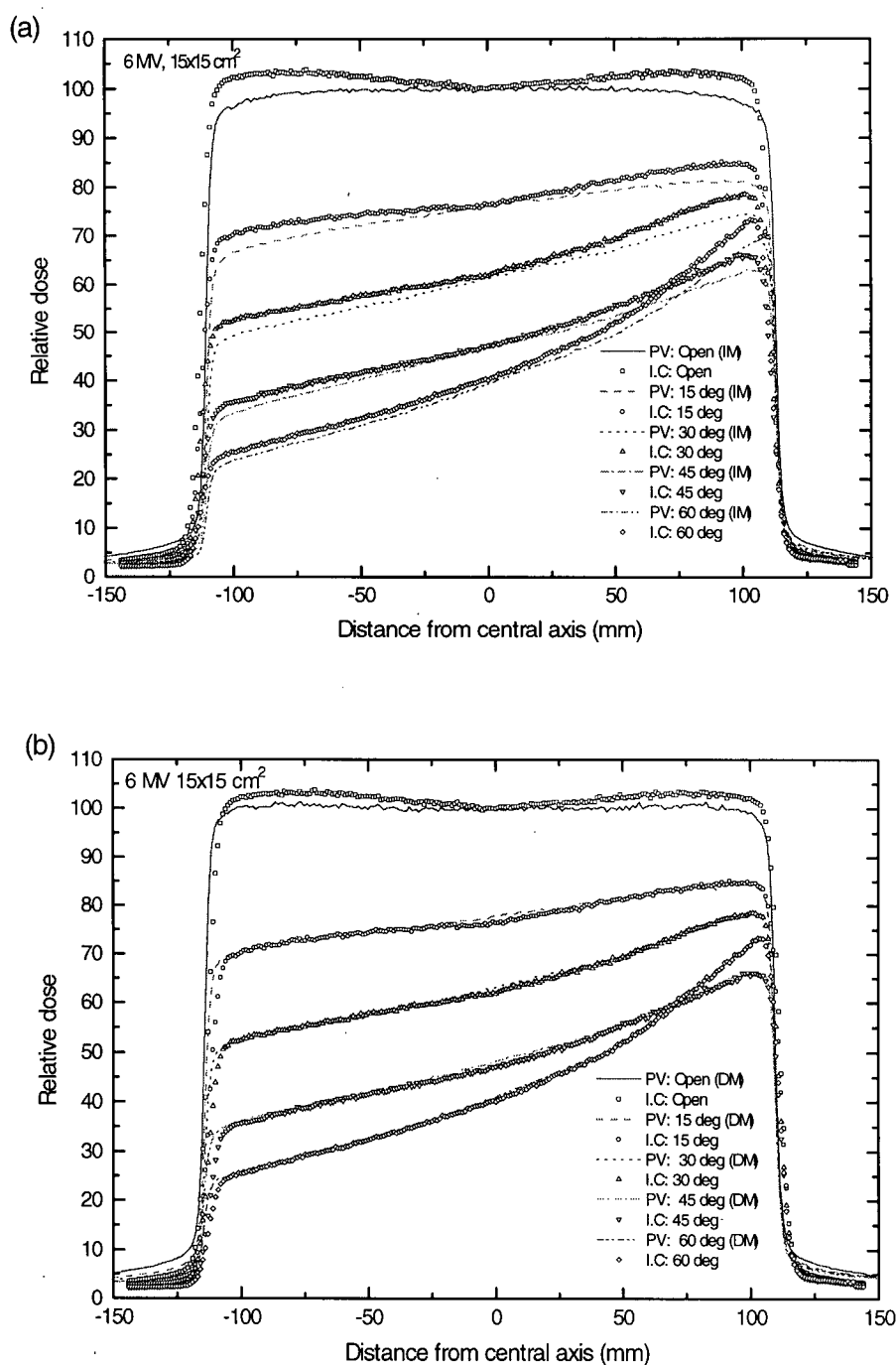


Figure 5.3: The comparison of portal dose profiles of ion chamber (I.C.) to Portal Vision™ (PV) in (a) imaging mode (IM) and (b) in dosimetric mode (DM) for 6 MV photons and 15x15 cm² field size is shown.

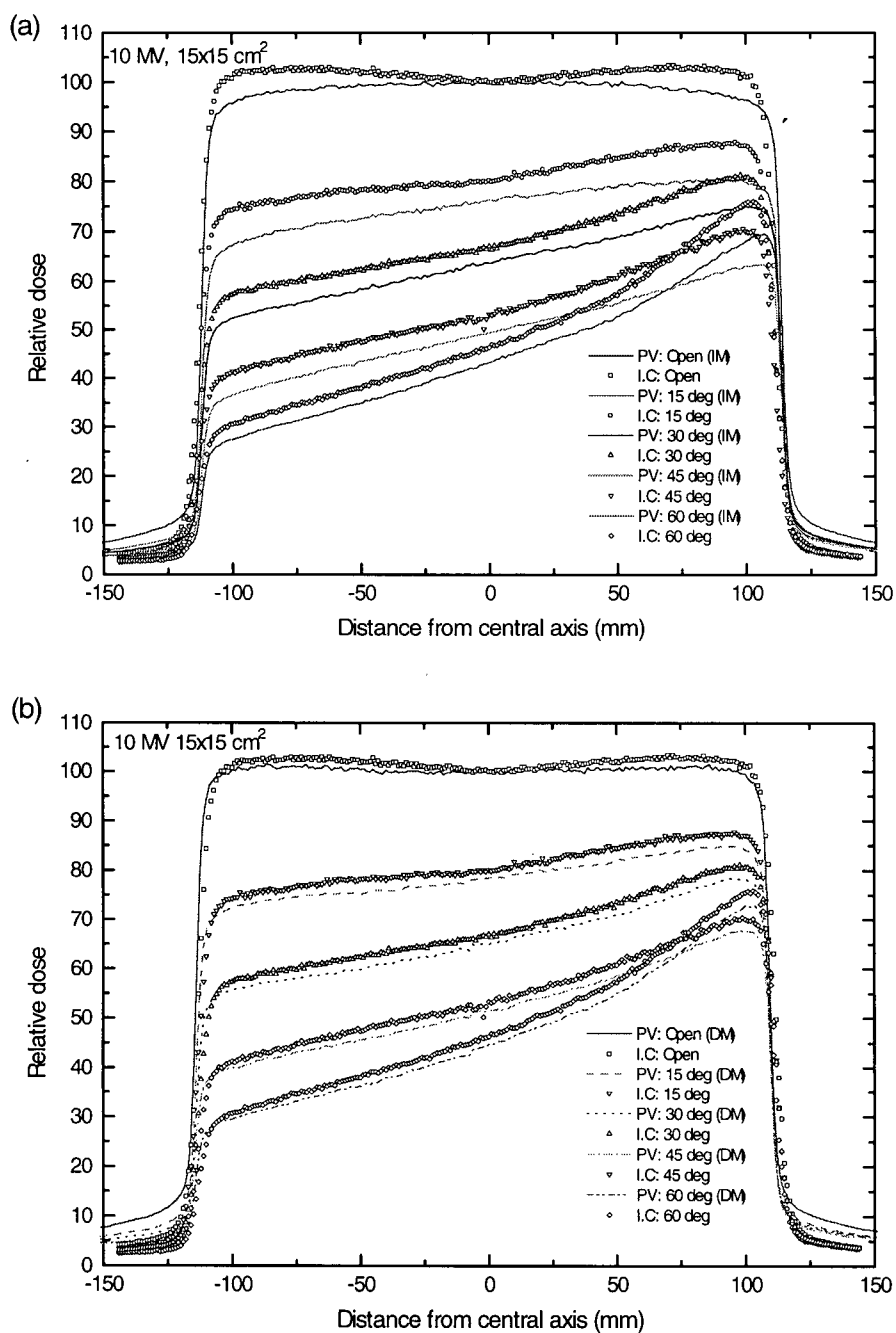


Figure 5.4: The comparison of portal dose profiles of ion chamber (I.C.) to Portal Vision™ (PV) in (a) imaging mode (IM) and (b) in dosimetric mode (DM) for 10 MV photons and 15x15 cm² field size is shown.

Table 5.3.1 summarizes the maximum percentage deviations between the ion chamber and the portal imager at the beam axis when calibrated for dosimetric mode for various field sizes and energies.

Table 5.3.1: The maximum percentage deviation of dose profiles at central axis between ion chamber and portal imager in dosimetric mode for the 6 and 10 MV beams and various field sizes are shown.

<i>Photon energy</i>	<i>6 MV</i>			<i>10 MV</i>		
<i>Field size (cm²)</i>	<i>5x5</i>	<i>10x10</i>	<i>15x15</i>	<i>5x5</i>	<i>10x10</i>	<i>15x15</i>
<i>15⁰ wedge</i>	0.0%	2.6%	1.0%	3.4%	2.0%	2.5%
<i>30⁰ wedge</i>	0.0%	1.0%	0.0%	2.9%	1.0%	2.9%
<i>45⁰ wedge</i>	0.6%	1.0%	0.0%	3.5%	3.0%	3.0%
<i>60⁰ wedge</i>	0.8%	1.0%	0.0%	3.0%	2.6%	2.8%

Comparison at central axis between the ion chamber and the imaging device in imaging mode showed no difference from Table 5.3.1. However, this variation becomes more pronounced and significant at the field edges as they are shown in Tables 5.3.2-4. when analyzed at 3, 6, and 10 cm from the central axis for field sizes of 5x5, 10x10, and 15x15 cm² respectively.

Table 5.3.2: The maximum deviations in dose at field edges (3 cm from the beam axis) between ion chamber and portal imager in both imaging and dosimetric modes for 5x5 cm² field size and two energies are shown.

<i>Photon energy</i>	<i>6 MV</i>		<i>10 MV</i>	
<i>Field size (cm²)</i>	<i>5x5 cm²</i>		<i>5x5 cm²</i>	
<i>System mode</i>	<i>Imaging mode (IM)</i>	<i>Dosimetric Mode (DM)</i>	<i>Imaging mode (IM)</i>	<i>Dosimetric mode (DM)</i>
<i>0⁰ (Open field)</i>	3.0%	1.0%	2.0%	0.0%
<i>15⁰ wedge</i>	3.0%	0.0%	8.0%	3.0%
<i>30⁰ wedge</i>	4.0%	0.0%	9.0%	3.0%
<i>45⁰ wedge</i>	3.0%	1.0%	7.0%	2.8%
<i>60⁰ wedge</i>	3.0%	1.0%	7.0%	3.0%

Table 5.3.3: The maximum deviations in dose at field edges (6 cm from the beam axis) between ion chamber and portal imager in both imaging and dosimetric modes for 10x10 cm² field size and two energies are shown.

<i>Photon energy</i>	<i>6 MV</i>		<i>10 MV</i>	
<i>Field size (cm²)</i>	<i>10x10 cm²</i>		<i>10x10 cm²</i>	
<i>System mode</i>	<i>Imaging mode (IM)</i>	<i>Dosimetric Mode (DM)</i>	<i>Imaging mode (IM)</i>	<i>Dosimetric mode (DM)</i>
<i>0° (Open field)</i>	6.0%	1.0%	5.0%	0.0%
<i>15° wedge</i>	6.0%	3.0%	8.0%	3.0%
<i>30° wedge</i>	8.0%	1.0%	8.0%	1.0%
<i>45° wedge</i>	7.0%	1.0%	11.0%	1.0%
<i>60° wedge</i>	8.0%	1.0%	12.0%	3.0%

Table 5.3.4: The maximum deviations in dose at field edges (10 cm from the beam axis) between ion chamber and portal imager in both imaging and dosimetric modes for 15x15 cm² field size and two energies are shown.

<i>Photon energy</i>	<i>6 MV</i>		<i>10 MV</i>	
<i>Field size (cm²)</i>	<i>15x15 cm²</i>		<i>15x15 cm²</i>	
<i>System mode</i>	<i>Imaging mode (IM)</i>	<i>Dosimetric Mode (DM)</i>	<i>Imaging mode (IM)</i>	<i>Dosimetric mode (DM)</i>
<i>0° (Open field)</i>	8.0%	2.0%	5.0%	0.0%
<i>15° wedge</i>	6.0%	0.0%	10.0%	2.0%
<i>30° wedge</i>	7.0%	0.0%	8.0%	2.4%
<i>45° wedge</i>	7.0%	0.0%	12.0%	2.0%
<i>60° wedge</i>	7.0%	0.0%	11.0%	2.0%

5.4 Discussion

For dosimetry applications, an additional build-up layer on top of the EPID's detector cassette is required to calibrate the system prior to any measurements. This is because, the imaging system corrects for large pixel to pixel variations across the detector for a given energy. However, the actual response of a standard dosimeter (ionization chamber) is different from that of SLIC. Therefore, to use the SLIC-EPID for dosimetric purposes, this sensitivity variation of the system is calibrated in a flat field. This was achieved by obtaining a series of ion chamber scans at various depths as shown in Fig. 5.1. to determine the optimal depth at which the beam intensity is uniform across the field of view (FOV). The calibration of the imaging system was then performed by placing a 10 cm perspex (water equivalent material) on the sensitive area of the imaging detector (32x32 cm²).

When dose profiles for open and wedged fields were obtained using both ionization chamber and the SLIC in dosimetric mode, it was shown that the imaging system can measure the transit dose to within 3.5% of the ion chamber results.

The wedged and open field dose profiles of portal imager both in dosimetric and imaging modes were compared at off axis regions (horns, a distance of 3, 6, and 10 cm from the central axis for 5x5, 10x10, and 15x15 cm² field sizes respectively). In dosimetric mode, the response of the imaging system was found to be within 3.0% of ion chamber results for all three field sizes. However, the results of portal imager in imaging mode deviated by as much as 12% from the ion chamber measurements.

In summary, one may draw the following conclusions; the variation in exit dose measurements at central axis obtained using the portal imager to those of ionization chamber is less than 3.5% which indicates the degree of system accuracy in determination of exit dose. This is good considering the ICRU report which recommends an overall accuracy of 5% in radiation dose delivery.³⁴

Chapter 6

Conclusions

6.1 Summary

On-line electronic portal imaging devices (EPIDs) have the potential to result in real benefits to patients receiving radiation treatments by providing near real time images which are used in geometric verification of radiation field size.^{14,15,24,38} In these systems, the radiation dose delivered on a given treatment can be used to produce a digital on-line image that is displayed in real or near-real time and hence enables the treatment operator to correct for any errors or geometrical misalignments that may arise in patient set-up. The current applications of on-line imaging devices are.³⁹ (1) Quantification of the position of anatomical structures within the radiation field. (2) To investigate effects of patient motion during one irradiation session and during a complete radiotherapy course. (3) Measurement of field size, and shape at the time of dose delivery. (4) To verify innovative treatments that require higher accuracy and to replace the conventional modality presently in use (portal film).

In radiotherapy, conventionally, the accuracy of dose delivered can be determined by *in-vivo* dosimetry in which diodes and TLD dosimeters are placed on the entrance and exit

surfaces of the patient during treatment. Exit dose measurements when combined with entrance dose measurements can provide a basis for understanding the dose distribution in the patient. Such spot checks, however, are useful in detecting errors in the absolute dose level at only few locations. To map a two dimensional dose distribution in the plane perpendicular to the beam axis, large area portal images are required as are provided by portal films.⁴⁰⁻⁴² However, due to the drawbacks of portal films described in Chapter 1, electronic portal imaging devices have the potential to become the ideal choice of *in-vivo* dosimetry in future. An advantage of EPIDs and portal films over diodes and TLDs is that they are capable of predicting the exit dose in two dimensions. Although exit dosimetry studies using films have been described,^{28,43} EPID images are preferred over the portal films because of their ease of image analysis, image storage, and on-line image acquisition.

A matrix of scanning liquid-filled ionization chamber electronic portal imaging device (SLIC-EPID) installed on a Varian Clinac[™] 2100C/D linear accelerator in our institute was investigated to determine its dosimetric characteristics. The prime objective of this work was to study the imaging device under various operating conditions and evaluate the system's capabilities for use as an alternative transit (exit) dosimeter.

In Chapter 3 of this thesis the characteristics curves of the SLIC-EPID in relation to the output incident radiation intensity were shown to be dependent on dose and could be characterized by a square root model.⁴² The dose response relationship on the central axis of the radiation beam could be described by this model to within 1% accuracy.

The characteristic curves (relationship between pixel values and dose) were studied by relating the incident radiation intensity to the output pixel values (ionization current) of the matrix of scanning liquid-filled ion chambers. Variation of radiation intensity was achieved by varying the source to detector distance. The dose response relation was also studied by changing the dose rate from 100 to 300 MU/min. From Figs. 3.2-3.4 it can be seen that for higher dose rates the response of the system becomes more linear with dose. Furthermore, the system response was studied with different collimated field sizes to determine any radiation field size dependence. It was found that the imaging detector has no significant dependence up to a collimated field size of $20 \times 20 \text{ cm}^2$ for both the 6 MV and the 10 MV beam. Therefore, for simplicity, it is safe to assume that the system is independent of field size for both nominal energies. The advantage of making such an assumption is that the measurements of exit dose for any given field size may be done by considering the parameters of the square root model for one given field size rather than determining the parameters for various field sizes.

In Chapter 4, the exit dose measurements were performed at the central axis of the beam with the SLIC. Phantom materials of various thicknesses, densities, and effective atomic numbers were used to simulate the attenuation of the beam which occurs clinically with various body parts. To compare the data obtained with the SLIC to actual exit dose measurements, a set of identical measurements were performed using a Farmer-type, 0.6 cm^3 cylindrical ionization chamber connected to an electrometer. It has been shown that, when the response of the system is corrected for its square root dependence to dose, the maximum percentage deviation at central axis between the two detectors response is less

than 3% for both the 6 and the 10 MV photon beams.⁴⁴ These results demonstrate the reproducibility of the SLIC in comparison to ion chamber dosimeters.

In Chapter 5, a description of the system calibration for use in dosimetric mode (DM) was presented and compared to ion chamber measurements. It was found that SLIC can underestimate the exit dose by as much as 12% at regions near the field edge if additional build-up material is not used in the calibration of the system. It was also found that the presence of additional build-up material for calibration purposes did not alter the image quality, which implies that the effect of beam hardening has no influence on image quality. However, Boellaard *et al.*³⁶ have found that for energies above 25 MV, the image quality tends to deteriorate in comparison to lower energies when build-up material is placed on top of the portal imager.

In conclusion, the scanning liquid-filled ion chamber imaging device, when used for dosimetry applications, requires additional build-up material for system calibration. The system is capable of measuring the transit (exit) dose to an accuracy of within 3.5%. This margin of error is acceptable, because, the objective of using the portal imager as an exit dosimeter is to determine the exit dose relative to the calculated dose. Furthermore, the method of system calibration for dosimetric application, presented in this thesis is far more practical for clinical applications than the method proposed by other investigators.³⁶ This is because, our system only needs a one time use of build-up material for the calibration of the imaging device, whereas, the later requires constant positioning of the build-up material on the imaging detector for each measurement which may be

problematic in measurements with, for instance, different gantry angles, or various source to detector distances.

Finally, it is important to emphasize that because of differences between accelerators (beam quality etc.) and between the individual EPIDs, it is necessary to measure the dose response relationship for each clinically applied combination EPID and accelerator setting to use the EPID for accurate dosimetric applications.

6.2 Future Work

In this study, the dosimetric characteristics of SLIC-EPID were examined under various conditions. However, not all clinical aspects of EPIDs are exhaustively investigated and well understood. Perhaps, further investigating the transmission dose rate measurements with phantoms containing inhomogeneities, simulating the variation in beam intensity which occurs clinically by various body parts, long term stability of the system's response due to temperature and radiation effects, and change in parameters such as gantry angle, acquisition mode, and more off axis measurements of exit dose would lead to recommendations that improve quality control in radiotherapy.

Finally developing an algorithm in which the system can be used in a clinical setting interchangeably as an integrated dosimeter as well as imaging device will be of interest.

References

1. De Neve, W., Van den Heuvel, F., De Beukeleer, M., Coghe, M., Thon, L., De Roover, P., Van Lancker, M., Storme, G., "*Routine clinical on-line portal imaging followed by immediate field adjustment using a tele-controlled patient couch*" Radiotherapy and Oncology, Vol. 24, pp. 45-54, 1992.
2. Reinstein L.E., Pai, S., Meek, A.G., "*Assessment of geometric treatment accuracy using time lapse display of electronic portal imaging*" Int. J. Rad. Onc. Biol. Phys., Vol. 22, pp. 1139-1146, 1992.
3. Karzmark, C. J., "*Advances in linear accelerator design for radiotherapy*" Medical Physics, Vol. 11, No. 2, pp. 105-128, 1984.
4. Marks, J. E., Haus, A. G., Sutton, H. G., Griem, M. L., "*The value of frequent verification films in reducing localization error in the irradiation of complex fields*" Cancer, Vol. 37, pp. 2755-2761, 1976.
5. Byhardt, R. W., Cox, J. D., Horngurg, A., Liermann, G., "*Weekly localization films and detection of field displacement errors*" Int. J. Rad. Onc. Biol. Phys., Vol. 4, pp. 881-887, 1978.
6. Marks, J. E., Davis, M. D., Haus, A. G., "*Anatomic and geometric precision in radiotherapy*" Radiobiology and Clinical Biology, Vol. 43, pp. 1-20, 1974.
7. Reinstein, L. E., Amols, H. I., Biggs, P. J., Droege, R. T., Filimonov, A. B., Lutz, W. R., Sholomo, S., AAPM Report No. 24, "*Radiotherapy portal imaging quality*" 1988.
8. Kirby, M. C., Williams, P.C., "*Measurement possibilities using an electronic portal imaging device*" Radiotherapy and Oncology, Vol. 29, pp. 237-243, 1993.

9. Siemens Medical Laboratories™ "*Beamview on-line portal imaging system*" Commercial Brochure.
10. Kesteloot, K., Dutreix, A., van der Schueren, E., "*A model for calculating the costs of in vivo dosimetry and portal imaging in radiotherapy departments*" Radiotherapy and Oncology, Vol. 28, pp. 108-117, 1993.
11. Boyer, A. L., Antonuk, L., Fenster, A., van Herk, M., Meertens, H., Munro, P., Reinstein, L. E., Wong, J. "*A review of electronic portal imaging devices (EPIDs)*" Medical Physics, Vol. 19, No. 1, pp. 1-16, 1992.
12. Verhey, L. V., Goitein, M., McNulty, P., Munzenrider, J. E., Suit, H. D., "*Precise positioning of patients for radiation therapy*" Int. J. Rad. Onc. Biol. Phys., Vol. 8, pp. 289-294, 1982.
13. Rabinowitz, I., Broomberg, J., Goitein, M., McCarthy, K., Leong, J., "*Accuracy of radiation field alignment in clinical practice*" Int. J. Rad. Onc. Biol. Phys., Vol. 11, pp. 1857-1867, 1985.
14. Kirby, M. C., Williams, P. C. "*The use of an electronic portal imaging device for exit dosimetry and quality control measurements*" Int. J. Rad. Onc. Biol. Phys., Vol. 31, No. 3, pp. 593-603, 1995.
15. Zhu, Y., Jiang, X. Van Dyk, J., "*Portal dosimetry using a liquid ion chamber matrix: Dose response studies*" Medical Physics, Vol. 22, No. 7, pp. 1101-1106, 1995.
16. Wong, J. W., Binns, W. R., Cheng, A., Epstien, J. W., Klarmann, J., Israel, M. H., Fenster, A., Purdy, J. A., "*On line radiotherapy imaging with an array of fiber-optic image reducers*" Int. J. Rad. Onc. Biol. Phys., Suppl., 1 15,201, (abstract), 1988.
17. Wong, J. W., Binns, W. R., Cheng, A. Y., Gear, L. Y., Epstein, J. W., Klarmann, J., Purdy, J. A., "*On-line radiotherapy imaging with an array of fiber-optic image reducers*" Int. J. Rad. Onc. Biol. Phys., Vol. 18, pp. 1477-1484, 1990.

18. Munro, P., Rawlinson, J. A., Fenster, A., "A digital fluoroscopic imaging device for radiotherapy localization" Proc. SPIE., 1090, pp. 321-329, 1989.
19. van Herk, M., Meertens H. "A matrix ionization chamber imaging device for on-line patient setup verification during radiotherapy" Radiotherapy and Oncology, Vol. 11, pp. 369-378, 1988.
20. van Herk, M., "Physical aspects of a liquid-filled ionization chamber with pulsed polarizing voltage" Medical Physics, Vol. 18, No. 4, pp.692-702, 1991.
21. Yin, F. F., Schell, M. C., Rubin, P. "Input/output characteristics of a matrix ion-chamber electronic portal imaging device" Medical Physics, Vol. 21, pp. 1447-1454, 1994.
22. Meertens, H., van Herk, M., Weeda, J., "A liquid ionization detector for digital radiography of therapeutic megavoltage photon beams" Phys. Med. Biol., Vol. 30, No. 4, pp. 313-321, 1985.
23. Webb, S., "The physics of three dimensional radiation therapy" Institute of Physics Publishing, Bristol and Philadelphia. pp. 246-290. 1993.
24. Swindell, W., Gildersleve, J., "Megavoltage imaging in radiotherapy" Rad. Magazine, Vol. 17, pp. 18-20, 1991.
25. Wong, J. W., Slessinger, E. D., Hermes, R. E., Offutt, C. J., Roy, T., Vannier, M. W., "Portal dose images I: Quantitative treatment plan verification" Int. J. Rad. Onc. Biol. Phys., Vol. 18, pp. 1455-1463, 1990.
26. Ying, X., Geer, L. Y., Wong, J. W., "Portal dose images II: Patient dose estimation" Int. J. Rad. Onc. Biol. Phys. Vol. 18, pp. 1465-1475, 1990.
27. Heukelom, S., Lanson, J. H., Mijnheer, B. J., "Comparison of entrance and exit dose measurements using ionization chambers and diodes" Phys. Med. Biol., Vol. 36, No. 1, pp. 47-59, 1991.

28. Fiorino, C., del Vecchio, A., Cattaneo, G. M., Fusca, M., Longobardi, B., Signorotto, P., Calandrino, R., "*Exit dose measurements by portal film dosimetry*" Radiotherapy and Oncology, Vol. 29, pp. 336-340, 1993.
29. Johns, H. E., Cunningham, J., "*The physics of radiology*" Thomas, Springfield, IL., 4th edition. 1983.
30. Khan, F. M., "*The physics of radiation therapy*" Williams & Wilkins, Maltimore, Maryland, 1994.
31. Wilks, R., "*Principles of radiological physics*" Churchill, Livingstone, New York, NY., 1981.
32. American Association of Physicists in Medicine. Radiation Therapy Committee, Task Group 21, "*A protocol for the determination of absorbed dose from high energy photon and electron beams*" Medical Physics, Vol. 10, pp. 741, 1983.
33. Sewchand, W., Khan, F., Williamson, J., "*Variation in depth dose data between open and wedge fields for 4 MV X-rays*" Radiology, 127, pp 789-792, 1978.
34. International Commission on Radiation Units and Measurements (ICRU) Report 24, "*Determination of absorbed dose in a patient irradiated by beams of X or γ rays in radiotherapy procedures*" Issued September 15, 1976.
35. Knoll, G. F., "*Radiation detection and measurement*" John Wiley & Sons, Inc. 1989.
36. Boellaard, R., van Herk, M., Mijnheer, B. J., "*The dose response relationship of a liquid-filled electronic portal imaging device*" Medical Physics, Vol. 23, No. 9, pp. 1601-1611, 1996.
37. Essers, M., Hoogervorst, B. R., van Herk, M., Lanson, H., Mijnheer, B. J., "*Dosimetric characteristics of a liquid-filled electronic portal imaging device*" Int. J. Rad. Onc. Biol. Phys., Vol. 33, No. 5, pp. 1265-1272, 1995.

38. Shalev, S., "Megavoltage portal imaging" Proceedings of the American Association of Physicists in Medicine (AAPM) summer school, June 1996.
39. Meertens, H. van Herk, M., Bijhold, J., Bartelink, H. "First clinical experience with a newly developed electronic portal imaging device" Int. J. Rad. Onc. Biol. Phys. Vol. 18, pp. 1173-1181, 1990.
40. van Dam, J., Vaerman, C., Blanckaert, N., Leunens, G., Dutreix, A., van der Schueren, E., "Are port films reliable for in vivo exit dose measurements?" Radiotherapy and Oncology, Vol. 25, pp. 67-72, 1992.
41. Fiorino, C., del Vecchio, A., Cattaneo, G. M., Fusca, M., Longobardi, B., Signorotto, P., Calandrino, R., "Exit dose measurements by portal film dosimetry" Radiotherapy and Oncology, Vol. 29, pp. 336-340, 1993.
42. Essers, M., Boellaard, R., van Herk, M., Lanson, H., Mijnheer, B., "Transmission dosimetry with a liquid filled electronic portal imaging device" Int. J. Rad. Onc. Biol. Phys., Vol. 34, No. 4, pp. 931-941, 1996.
43. Huyskens, D., Van Dam, J., Dutreix, A., "Midplane dose determination using in vivo dose measurements in combination with portal imaging" Phys. Med. Biol. Vol 39, pp. 1089-1101, 1994.
44. Parsaei, H., El-Khatib, E., Rajapakshe, R., "Exit dosimerty using an EPID for megavoltage photon beams" Medical Physics Vol 23, No. 5, p. 802, (abstract), 1996.

Appendix 1

This program was written in C code to extract uncompressed pixel values of the portal imager for graphical and other computational analysis of the output values of the imaging device.

```
/*      Portal Vision image analysis program:
```

```
      This program reads Varian uncompressed image files and saves
      average rows or columns as new files for image analysis.      */
```

```
#include <stdio.h>
#include <conio.h>
#include <malloc.h>
#include <process.h>
#include <math.h>
#include <stdlib.h>
```

```
short *pic[256];      /* pointer to WORD picture buffer */
void main(void)
```

```
{
```

```
    FILE *in, *data;
    int k;
    int row;
    int column;
    char choice;
    char imfile[100], outdata[100];
    unsigned char header[1024];
    fflush(stdin);
```

```
    printf("\n Enter filename of the image to be analyzed: ");
    fflush(stdin); /* It "flushes" the buffer after each operation */
    scanf("%s",imfile);
```

```

fflush(stdin);

while(1)
{
printf("\n Do you want to analyze rows or columns ?");
printf("\n");
printf("\n Enter 'r' for reading rows, or 'c' for reading columns:");
fflush(stdin);
scanf("%c",&choice);
fflush(stdin);
if(choice == 'r' || choice == 'R')
{
/* Specifications of the image under analysis */

printf("\n Enter the row number(0-256):");
fflush(stdin);
scanf("%d",&row);
printf("\n Enter the new filename of row data:");
fflush(stdin);
scanf("%s",outdata);
break;
}
else if(choice == 'c' || choice == 'C')
{
printf("\n Enter the column number (0-256):");
scanf("%d",&column);
fflush(stdin);
printf("\n Enter the new filename of column data :");
fflush(stdin);
scanf("%s",outdata);
fflush(stdin);
break;
}
else printf("wrong choice, try again BUD!!\n");
}

/* open image file in "read binary" mode: */

if( (in = fopen(imfile,"rb")) != NULL) {

/* read header into buffer */

fread ( header,sizeof(char),1024,in );
/* allocate line buffer memories for image */
for ( k=0; k<256; k++){

```

```

pic[k] = (short*)malloc(256*sizeof(short));

if (pic[k]==NULL) {

printf(" Not enough memory to allocate buffer!\n");
fclose(in);
exit(0);      /* terminates program if out of memory */

}

}

for ( k=0; k<256; k++) {

        /* Read image data into pic[] */

        fread ( pic[k], sizeof(short), 256, in );
        }
fclose(in);

}

else {
    perror("read error");
    exit(0);
}

        /* Open a new file for writing data */

if((data = fopen(outdata,"w")) == NULL) {

    printf(" Not enough memory, cannot open\n");
    exit(0);      /* terminate the program and exit */

}

for(k=0;k<256;k++){
    if(choice == 'r'){

        /* Show the 5 rows of pixel values on the screen */

printf("\%d %d %d %d %d\n", *(pic[row]+k), *(pic[row+1]+k),
*(pic[row+2]+k), *(pic[row+3]+k), *(pic[row+4]+k));

        /* Take the average of 5 rows and "dump" them into the new file */

```

```

        fprintf(data,"%f \n",(float)(*(pic[row]+k)+ *(pic[row+1]+k)+
        *(pic[row+2]+k)+ *(pic[row+3]+k)+ *(pic[row+4]+k))/ (-5.0));
    }
    else {

        /* Show the five columns of pixel values on the screen */

        printf("\nd %d %d %d %d \n", *(pic[column]+k), *(pic[column]+k+1),
        *(pic[column]+k+2), *(pic[column]+k+3), *(pic[column]+k+4));

        /* take the average of 5 columns and "dump" them into the new file */

        fprintf(data,"%f \n",(float)(*(pic[column]+k)+ *(pic[column]+k+1)+
        *(pic[column]+k+2)+ *(pic[column]+k+3)+ *(pic[column]+k+4))/ (-5.0));

    }

}

fclose(data);

        /* Free the buffers */

for ( k=0; k<256; k++ ) {
    free(pic[k]);
}

}

```